Mathematical and Computational Applications

MDPI

Article

Using Artificial Neural Network Analysis to Study Jeffrey Nanofluid Flow in Cone–Disk Systems

Nasser Nammas Albaqami

Department of Information Technology, King Abdulaziz University, Jeddah 21589, Saudi Arabia; nalbugami@kau.edu.sa

Abstract: Artificial intelligence (AI) is employed in fluid flow models to enhance the simulation's accuracy, to more effectively optimize the fluid flow models, and to realize reliable fluid flow systems with improved performance. Jeffery fluid flow through the interstice of a cone-and-disk system is considered in this study. The mathematical description of this flow involves converting a partial differential system into a nonlinear ordinary differential system and solving it using a neurocomputational technique. The fluid streaming through the disk–cone gap is investigated under four contrasting frameworks, i.e., (i) passive cone and spinning disk, (ii) spinning cone and passive disk, (iii) cone and disk rotating in the same direction, and (iv) cone and disk rotating in opposite directions. Employing the recently developed technique of artificial neural networks (ANNs) can be effective for handling and optimizing fluid flow exploits. The proposed approach integrates training, testing and analysis, and authentication based on a locus dataset to address various aspects of fluid problems. The mean square error, regression plots, curve-fitting graphs, and error histograms are used to evaluate the performance of the least mean square neural network algorithm (LMS-NNA). The results show that these equations are consistently aligned, and agreement is, on average, in the order of 10^{-8}. While the resting parameters were kept static, the transverse velocity distribution, in all four cases, exhibited an incremental decreasing behavior in the estimates of magnetic and Jeffery fluid factors. Furthermore, the results obtained were compared with those in the literature, and the close agreement confirms our results. To train the model, 80% of the data were used for LMS-NNA, with 10% used for testing and the remaining 10% for validation. The quantitative and qualitative outputs obtained from the neural network strategy and parameter variation were thoroughly examined and discussed.

Keywords: Jeffrey fluid flow; devices consisting of cones and disks; artificial neural network (ANN); study of heat transfer; Buongiorno model

Citation: Albaqami, N.N. Using Artificial Neural Network Analysis to Study Jeffrey Nanofluid Flow in Cone–Disk Systems. *Math. Comput. Appl.* **2024**, *29*, 98. https://doi.org/10.3390/mca29060098

Academic Editor: Mehmet Pakdemirli

Received: 21 July 2024
Revised: 9 October 2024
Accepted: 14 October 2024
Published: 31 October 2024

1. Introduction

A certain class of non-Newtonian fluids, characterized by their stress–relaxation attributes, cannot be described using viscous models. The Jeffery fluid model best captures the non-Newtonian nature of such media with a characteristic memory time scale, also known as relaxation time. It was first proposed by H. Jeffery in 1922. A Jeffery fluid is characterized by its elasticity, which makes it suitable for applications involving heat transfer.

Jeffery fluids are commonly used in polymer processing, such as plastic extrusion and injection molding. Khadrawi et al. [1] studied basic viscoelastic fluid flow problems using the Jeffery model. The elasticity of Jeffery fluids helps in the efficient transfer of heat during melting and molding processes. A Jeffery fluid can be used as a heat transfer medium in heat exchangers, where the non-Newtonian behavior of the fluid enhances the heat transfer rate, leading to improved efficiency. Jeffery fluids are also used in the food-processing industry, especially in processes, like the mixing, heating, and cooling of various food products. Their elasticity allows for precise temperature control and uniform heat distribution during cooking, baking, and other food-processing operations. Hayat

et al. [2] analyzed peristaltic transport for the flow of a Jeffrey fluid. Jeffery fluids are used in solar energy systems, such as solar water heaters and solar thermal power plants. Their non-Newtonian behavior enhances heat transfer efficiency in heat storage systems and heat exchangers, maximizing the utilization of solar energy.

The cone-and-disk system has a wide range of practical and technical applications across diverse domains. These applications encompass the precise control of fluid distribution through the deployment of conical diffusers, the precise measurement of viscosity via viscometers, and its contribution to the advancement of medical devices, as broadly documented in citation [3]. The study of heat transfer in the context of fluid flow through the gap formed by a cone and a disk is of paramount significance, marked by its complexity and wide-ranging relevance across engineering and scientific developments [4]. This unique configuration plays a pivotal role in crucial industrial processes, including heat exchangers and mixing devices, while also serving as a fundamental component in rheological studies [5]. Its versatile applications underscore its significance as a focal point of research and innovation. Gul et al. [6] studied fluid flow in the canonical region of cone–disk geometry by taking into account two consistent constituents and two inconsistent constituents. The authors demonstrated that cooling is optimized for this setup when the disk rotates and the cone remains static under meticulously maintained conditions of uniform superficial temperature. Srilatha et al. [7] elaborated on thermal and concentric transportations for fluid streaming through the cone-and-disk system and discussed the thermophoretic motion of particles. They also proved that thermal transportation improves when the cone is fixed and the disk revolves. A nanofluid flow induced by a cone-and-disk system was studied by Moatimid et al. [4]. Their study revealed decreasing patterns in both the temperature and radial velocity, while the azimuthal velocity corresponded to auspicious effects. Regarding the mechanical system of a cone-and-disk setup, thermal exchange between the fluid and surfaces is one of the most salient considerations [8,9]. In recent decades, this phenomenon has gained much attention in various engineering, technological, and industrial applications, such as heat exchange systems, mixers, and various rheological studies [10].

Jeffrey fluids are in a class of non-Newtonian fluids characterized by a unique combination of both viscous (fluid-like) and elastic (solid-like) behaviors when subjected to deforming stresses. Due to their viscoelastic nature, these fluids show nonlinear sensitivity to tangential stresses and can be influenced by factors such as the rate of distortion. These heat-transferring media are incorporated into complex flow geometries in various fields of engineering and chemical, thermal, and applied sciences. The response of Jeffrey fluid streaming to various influencing sources is mathematically described with a non-Newtonian framework known as the Jeffrey fluid model [11]. In contrast to Newtonian law, which exhibits linear regression between shear stresses and deformations, the Jeffery fluid model demonstrates the viscoelastic attributes of a medium through its shear-thinning behavior and can be implemented as an appropriate tool in rheological analysis, polymer processing, and biological modeling [12–14]. Agarwal et al. [15] used computational analysis to analyze the viscoelastic fluid flow on an extending sheet immersed in a porous medium and characterized by micro-rotational and thermal radiative effects. As a result, they highlighted the unfavorable effects of Jeffery flow parameters and porosity parameters on fluid flow and heat transfer rates. In addition, the influence of expanding boundaries in a porous space on viscoelastic fluids was examined in [16]. The authors observed the velocity distribution to be an increasing function of the Jeffery factor. Regarding the thermal performance using Newtonian and non-Newtonian fluid models, optimizing the thermal transportation through various materials has attracted tremendous attention; see [17–19] and the references therein.

State-of-the-art artificial neural networks (ANNs) represent a novel breakthrough in the fields of intelligent retrieval, robotics, machine learning, and cybernetics [20]. Currently, their promising reliability and efficiency for multi-argument mathematical problems have encouraged researchers to logically optimize and simulate complex fluid flows in various

departments of fluid dynamics and mechanical engineering [21]. One of the significant advantages of ANNs is their ability to precisely model the complicated supervising correlations of fluid simulations, which are based on several flow inputs covering physical parameters, boundary constraints, and stream patterns. An extensive dataset is processed through hidden neural layers to forecast meaningful variations in fluid streaming and provide a complete insight picture of fluid dynamics [22]. In addition, the privilege of ANNs is their generalized feasibility, regardless of whether the arguments are sparse or turbulent. The design phase of the scheme involves meticulously networking the base frameworks, selecting the mathematical activation functions, and developing schematic algorithms to supplement the certainty and robust structure of ANN models. However, the incorporation of domain expertise and the integration of ANNs with physical frameworks can enhance their efficiency in addressing a broad spectrum of vicious flow optimization problems in practical engineering applications [23]. Recent research trends are almost all focused on ANNs [24–29].

The interaction between fluid dynamics and particle behavior is complex due to the effects of the Brownian and thermophoretic diffusivity of suspended particles in fluid flow [30]. On one hand, Brownian motion is a stochastic process defined as the random diffusion of particles suspended in a fluidic medium as a result of thermal agitation and governs many mechanisms, such as mixing processes, particle dynamics, and cellular motion. On the other hand, thermophoresis, also called the Soret effect, is referred to in particle dynamics in response to the temperature gradient, with a direct dependency on the particles and the medium's morphology. These phenomena can significantly influence the local temperature and concentric distributions of coarse-grained particles in deformable space, leading to an augmented dispersion of concentration and thermal convection. The simultaneous consequences of these phenomena yield a complex coupled formulation of particle–fluid interaction, making pivotal contributions to important fields, including those involving thermal, mechanical, industrial, biological, aerosol, colloidal, and nano mechanisms, where aptly handling particle dynamics through fluidic streams provides a basis for the comprehension and optimization of these phenomena and their exploitable applications [31–39].

To tackle problems that have been difficult to handle in most areas of applied science, researchers have used artificial intelligence-based computer solver applications. The application of artificial neural networks (ANNs) has become more common in science and engineering fields, such as fluid mechanics, where artificial intelligence (AI) has been proven to be beneficial. In fluid mechanics and other fields, such as aviation, automotive industries, and weather prediction, using AI is essential for predicting fluid flow patterns. For many challenges in several fields, such as nonlinear circuits, nuclear physics, thermodynamics, astrophysics, and magnetohydrodynamics (MHD), scholars have been able to estimate solutions using computational methods based on ANNs and the learning samples of supervised and/or unsupervised techniques. Examples of this include the transport model [6], COVID-19 models [40,41], and fluid dynamics [42]. According to the studies mentioned above, intelligent computing techniques that use ANNs can handle fluid mechanics-related problems.

The above considerations and literature review reveal that no efforts have been made regarding Jeffrey fluid flows in the canonical separation of a cone-and-disk system (CDS); thus, this serves as the primary motivation for our current investigation. In considering Jeffrey nanofluid flow in a cone-and-disk system for the first time, this study aims to address the following aspects:

(i) The Jeffrey fluid model is an essential part of heat transfer processes because it provides a precise description of the non-Newtonian and elastic behaviors of fluids, which have not yet been studied with the cone-and-disk geometry.
(ii) Studies in the literature have been restricted to a general model that takes into account a Newtonian fluid. In this study, four different scenarios are studied: (i) a static cone

and rotating disk, (ii), a static disk and rotating cone, (iii) the cone and disk rotating in the same direction, and (iv) the devices rotating in opposite directions.

(iii) Brownian diffusivity and the thermophoresis mechanism are used to regulate the thermal performance. These have not been studied for this particular system in terms of a Jeffrey fluid model.

(iv) ANN analysis, a new technique, is used to solve this kind of complex model.

2. Problem Formulation

A Jeffery fluid streaming through the region within a cone–disk system is considered herein. Mathematically, the flow configuration is described using the cylindrical framework $(r,\ \theta,\ z)$, with $r,\ \theta,$ and z symbolizing the horizontal (radial), azimuthal, and normal (axial) orientations, respectively, whereas geometrically, the disk is oriented at $z = 0$ and the cone is assembled at $z = r\tan\gamma$, with γ as the separation angle between the constituents. Meanwhile, the CDS is allowed to rotate axially with angular velocities ω and Ω, respectively. The effect of the simultaneous motion of the cone and disk on fluid flow is investigated while considering the following four distinct scenarios: (i) allowing the disk to rotate while the cone is stationary, (ii) allowing the cone to spin while the disk is held at rest, (iii) both the cone and disk gyrating in parallel directions, and (iv) both the cone and disk gyrating in opposite directions. In addition, the thermal performance, adhering to the superficial boundaries, is examined for the consequences of Brownian motion and the thermophoresis process. Unsteady streaming confined to $0 \le z \le r\tan\gamma$ is illustrated in Figure 1.

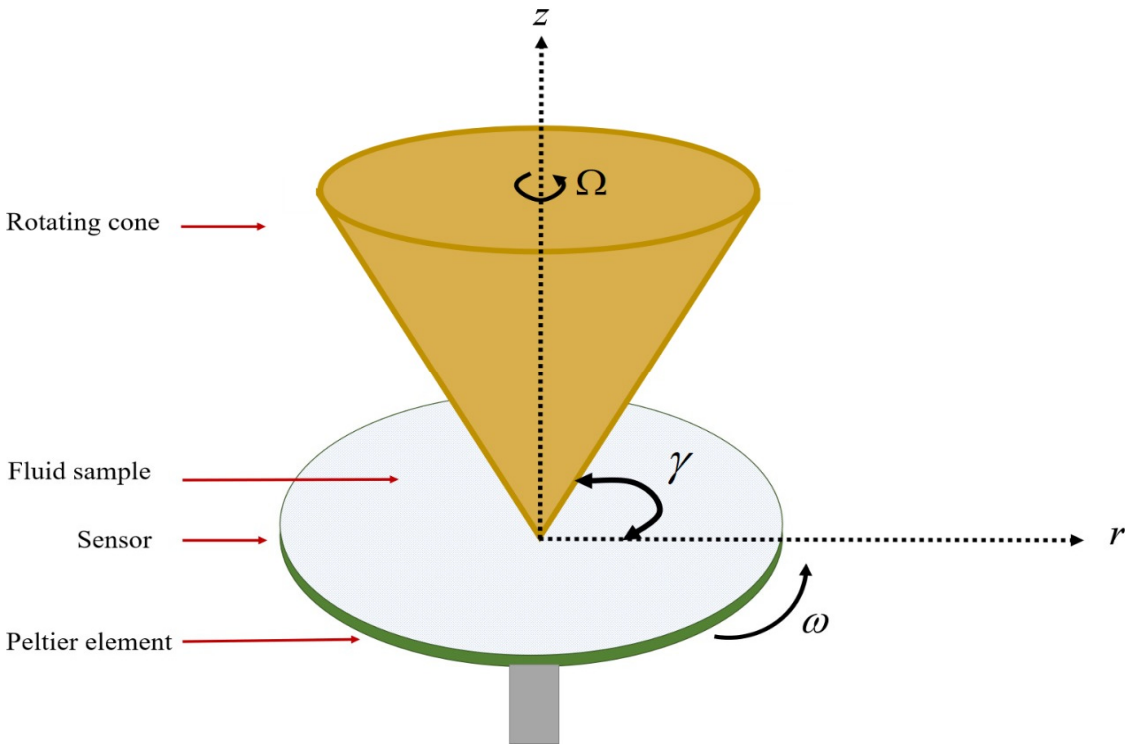

Figure 1. Physical interpretation of cone–disk geometry.

Assimilating the above-mentioned assumptions and considerations, the governing model yields the following [3,4,42–44]:

$$\partial_r u + ur^{-1} + \partial_z w = 0, \tag{1}$$

$$u\partial_r u + w\partial_z u - v^2 r^{-1} = -\partial_r p + \tfrac{v}{1+\lambda_1}\left(\partial_{rr}u + r^{-1}\partial_r u - ur^{-2} + \partial_{zz}u\right) - \tfrac{\lambda^*}{1+\lambda}\left(\begin{array}{l} 2u\partial_{rrr}u + 2w\partial_{rzz}u + 2\partial_r u\partial_{rr}u + 2\partial_r w\partial_{rz}u - 2ur^{-2}\partial_r u - 2wr^{-2}\partial_z u - 2u^2 r^{-3} \\ +\partial_z u\partial_{rr}w + \partial_z w\partial_{rz}w + 2u\partial_{rzz}u + 2w\partial_{zzz}w + \partial_z u\partial_{rz}u + \partial_z w\partial_{zz}u \end{array}\right), \quad (2)$$

$$u\partial_r v + w\partial_z v - uvr^{-1} = \tfrac{v}{1+\lambda_1}\left(\partial_{rr}v + r^{-1}\partial_r v - vr^{-2} + \partial_{zz}v\right) - \tfrac{\lambda^*}{1+\lambda}\left(\begin{array}{l} 2u\partial_{rrr}v + 2w\partial_{rrz}v - wr^{-2}\partial_z v + \partial_r u\partial_{rr}v + \partial_r w\partial_{rz}v - r^{-1}\partial_r u\partial_r v + vr^{-2}\partial_r u \\ -2uvr^{-3} - r^{-1}\partial_r w\partial_z v + 2u\partial_{rzz}v + 2w\partial_{zzz}v + \partial_z u\partial_{rz}v + \partial_z w\partial_{zz}v \end{array}\right), \quad (3)$$

$$u\partial_r w + w\partial_z w = -\partial_z p + \tfrac{v}{1+\lambda_1}\left(\partial_{rr}w + r^{-1}\partial_r w + \partial_{zz}w\right) - \tfrac{\lambda^*}{1+\lambda}\left(\begin{array}{l} 2u\partial_{rrr}w + u\partial_{rrz}u + w\partial_{rzz}u + 2w\partial_{rrz}w + \partial_r u\partial_{rz}u + \partial_r w\partial_{zz}u + \partial_r u\partial_{rr}w \\ +\partial_r w\partial_{rz}w + ur^{-1}\partial_{rr}w + wr^{-1}\partial_{rz}w + 3u\partial_{rzz}u + 3w\partial_{zzz}w + 2\partial_z u\partial_{rz}w + 2\partial_z w\partial_{zz}w \end{array}\right), \quad (4)$$

$$u\partial_r T + w\partial_z T = \alpha\partial_{zz}T + 2\tau\frac{D_T}{T_\infty}(u\partial_z T\partial_{rz}T + w\partial_z T\partial_{zz}T) + \tau\left(D_B(\partial_z C\partial_z T) + \frac{D_T}{T_\infty}(\partial_z T)^2\right), \quad (5)$$

$$u\partial_r C + w\partial_z C = D_B\partial_{zz}C + \frac{D_T}{T_\infty}(u\partial_{rzz}T + w\partial_{zzz}T) + \frac{D_T}{T_\infty}\partial_{zz}T, \quad (6)$$

with the following boundary constraints:

$$\begin{array}{l} u = \ w = 0, \ v = \omega\, r, \ T = T_w\,, \ C = \ C_w, \ \ at \ \ \mathrm{z} \ = \ 0, \\ u = w = 0, \ v = \Omega\, r, \ T = T_\infty\,, \ C = C_\infty, \ at \ z = r\tan\gamma. \end{array} \quad (7)$$

In Equations (1)–(7), $(u,\ v,\ w)$, p, T, and C represent the velocity components along the $(r,\ \theta,\ z)$ directions, pressure, temperature, and concentration, respectively. In addition, λ^* and λ denote the corresponding delay and relaxation times, while $v = \frac{\mu}{\rho}$, $\alpha = \frac{k}{\rho c_p}$, D_B, and D_T denote the momentum, thermal, Brownian, and thermophoresis diffusivities, where ρ, μ, k, and ρc_p signify the density field, dynamic viscosity, thermal conductivity, and heat capacity of the Jeffrey fluid, accordingly. The subscripts $_w$ and $_\infty$ are used to denote the relative boundary constraints.

For similarity equations, consider the following transformation:

$$\begin{array}{l} u = v_f\frac{f(\eta)}{r} = \mathrm{U}_w\, f(\eta),\ v = v_f\,\frac{g(\eta)}{r} = \mathrm{U}_w g(\eta),\ w = v_f\frac{h(\eta)}{r} = \mathrm{U}_w h(\eta), \\ \mathrm{p} = \frac{\rho v_f^2 P}{r^2} = \mathrm{U}_w^2\rho P,\ \eta = \frac{z}{r},\ T = T_\infty + \Theta(T_w - T_\infty),\ \ C = C_\infty + \phi(C_w - C_\infty). \end{array} \quad (8)$$

where U_w is used to show the surface velocity. Using Equation (8) in Equations (1)–(6), we obtain the following:

$$\begin{array}{l} \left(1+\eta^2\right)f'' + 3\eta f' + (1+\lambda)\left(\eta f f' - hf' + f^2 + g^2\right) \\ -\lambda_1\left[\begin{array}{l} 2(f)^3 + 4\eta f'\, f^2 + \eta^2 f^2 f'' + h^2 f'' - g^2 f - \eta g^2 f' \\ -4hff' - 2\eta hff'' + 2fg^2 + 2\eta fgg' - 2hgg' + fg^2 \end{array}\right] = 0, \end{array} \quad (9)$$

$$\begin{array}{l} (1+\eta)g'' + 3\eta f' - (1+\lambda)(\eta f g' + hg' + 2gf) \\ -\lambda_1\left[\begin{array}{l} 4\eta g' f^2 + \eta^2 g'' f^2 - 4hgg' - 2\eta hgg'' + \\ g^2 g'' - 2gf^2 + 2\eta gff' - \eta g' g^2 \end{array}\right] = 0, \end{array} \quad (10)$$

$$\begin{array}{rl} \left(1+\eta^2\right)h'' & +(1+\lambda)(3\eta f\, h' + \eta h' f - h(h' - 1 - f)) \\ & -\lambda_1\left[\begin{array}{l} 2hf^2 + \eta^2 hf^2 + \eta^2 h'' f^2 - h'' h^2 \\ -4hfh' - 2\eta hfh'' - hg^2 - \eta hg^2 \end{array}\right] = 0, \end{array} \quad (11)$$

$$\left(1+\eta^2\right)\Theta'' + \eta\Theta' - \mathrm{Pr}(h - \eta f)\Theta' + \left(1+\eta^2\right)\mathrm{Pr}N_b\Theta'\Phi' + \left(1+\eta^2\right)\mathrm{Pr}N_t\left(\Theta'\right)^2 = 0, \quad (12)$$

$$\left(1+\eta^2\right)\Phi'' + \eta\Phi' - Sc(h - \eta f)\Phi' + \frac{Nb}{Nt}\left(\left(1+\eta^2\right)\Phi'' + \eta\Phi'\right) = 0. \quad (13)$$

Below is an explanation of the boundary constraints in their transfer form:

$$\begin{array}{l} f(0) = h(0) = 0, \quad g(0) = \mathrm{Re}_\omega, \quad \Theta(0) = \Phi(0) = 1, \\ f(\eta_0) = h(\eta_0) = 0, \quad g(\eta_0) = \mathrm{Re}_\Omega, \quad \Theta(\eta_0) = \Phi(\eta_0) = 0. \end{array} \tag{14}$$

Here, $\lambda_1 = \frac{\lambda^* {U_w}^2}{v_f}$ is the relaxation time parameter, λ is the delay parameter, $Nt = \frac{\tau D_T \nabla T}{v_f T_\infty}$ = the thermophoresis factor, $Nb = \frac{\tau D_B \nabla C}{v_f}$ = the Brownian motion factor, $\mathrm{Pr} = \frac{\mu_f (c_p)_f}{k_f}$ = the Prandtl number, $Sc = \frac{v_f}{D_B}$ = the Schmidt number, $\mathrm{Re}_\Omega = \frac{r^2 \Omega}{v_f}$ = the local Reynolds number at the cone surface, and $\mathrm{Re}_\omega = \frac{r^2 \omega}{v_f}$ = the local Reynolds number at the disk surface.

Quantities of Interest

The primary parameters with salient implications for predicting the corresponding fluid transfer, heat transfer, and mass transfer rates include the local radial and tangential skin friction (denoted by C_f and C_g, respectively), local Nusselt number (Nu), and local Sherwood number (Sh). These quantities are mathematically expressed as

$$\left.\begin{array}{l} C_{f_{d,c}} = \frac{\tau_r}{\rho_f {U_w}^2}, \text{ where } \tau_r = \frac{\mu_f}{1+\lambda_1}\left[\partial_z u + \lambda_2 (u \partial_{rz} u + v \partial_{zz} u)\right]_{z=0,\ r\tan\gamma} \\ C_{g_{d,c}} = \frac{\tau_\theta}{\rho_f {U_w}^2}, \text{ where } \tau_\theta = \frac{\mu_f}{1+\lambda_1}\left[\frac{\partial v}{\partial z} + \lambda_1 (v \partial_{rz} v + u \partial_{zz} v)\right]_{z=0,\ r\tan\gamma} \end{array}\right\}, \tag{15}$$

$$\left.\begin{array}{l} Nu_{d,c} = \frac{r q_w}{k_f (T_w - T_\infty)}, \text{ where } q_w = -k_f (\partial_z T)\big|_{z=0,\ r\tan\gamma} \\ Sh_{d,c} = \frac{r J_w}{D_B (T_w - T_\infty)}, \text{ where } J_w = -D_B (\partial_z C)|_{z=0,\ r\tan\gamma} \end{array}\right\}, \tag{16}$$

respectively, where the symbols d and c describe the localized quantities in the vicinity of the disk $(z = 0)$ and cone $(z = r\tan\gamma)$, respectively.

3. Framework of Artificial Neural Networks (AANs)

The goal of artificial neural networks (ANNs) is to replicate biological neural networks, and ANNs were recently established as a hybrid machine learning algorithm (MLA). Over the last few years, the supervised learning algorithm (SLA), one of the three variants of MLAs, has emerged as a promising tool for the mathematical and statistical simulation of models, inspiring various applications in applied sciences because their handling process shares similarities with human brain algorithms. Artificial neurons, also known as nodes or numerical units, are represented in SLAs through edges that resemble the structure of neurons and synapses. A prototype called the multilayer perceptron (MLP) network has flourished for its ability to model convoluted functions using the most common ANN design. An SLA is a multilayered structure of input and output layers that are interlinked through a hidden layer, performing the required computations and displaying the outcomes, whilst weight adjustments are made through backpropagation.

The Levenberg–Marquardt learning algorithm (LMLA) is used to support the backpropagation neural network (BPNN), abbreviated as LMLA-BPNN, and is a training process involving an input signal that uses neural networks (NNs). The LMLA is specifically designed to minimize sum-of-square error expressions. Upon introducing an input pulse (a training or sample dataset), the comprehensive insight is stored within inter-neural links, known as "strengths" or "corresponding edges", which are supervised by associative networks of hidden films called "weights". Iteratively, these weights, which are considered two-dimensional arrays, are called upon when an input is fed to the NN to assess its estimates (output), providing a new testing input for the forthcoming iteration. The LMLA-BPNN is structured as an "input layer" that receives an input pulse (a training or sample dataset) introduced to the NN and is assembled into a "hidden layer", where the basic units responsible for simulation employ a systematic arrangement of "weighted

connections", to which the output layer is coupled, returning the final result. The effective minimization of errors is achieved through an iterative assessment of the LMLA-BPNN. To estimate the behavior of viscoelastic fluid flow in CDS geometry, the LMS-NNA, which implements the proposed ANN, is employed in this study. Moreover, weight adjustments are backpropagated and constructed using analogies and the interdependence of the yield target.

An ANN algorithm is used to envision the efforts of $g(\eta)$ against the Jeffrey fluid factor λ and magnetic parameter M while considering the four cases under consideration, i.e., (i) $\mathrm{Re}_{\Omega} = 1$, $\mathrm{Re}_{w} = 0$, (ii) $\mathrm{Re}_{\Omega} = 0$, $\mathrm{Re}_{w} = 1$, (iii) $\mathrm{Re}_{\Omega} = 2$, $\mathrm{Re}_{w} = 1$, and (iv) $\mathrm{Re}_{\Omega} = 1$, $\mathrm{Re}_{w} = -1$. Since the apt optimization of the dataset, which is employed for training mechanisms, is directly dependent on the anticipation certainty of the ANN, the LMLA-BPNN is successfully incorporated.

Optimizing the data used during development is vital for the ANN technique to provide precise estimates [45]. The testing phase uses 10% of the data, while the validation phase uses 10%, and the outstanding 80% is used to train the ANN to its full potential. The development of the ANN model requires meticulous data optimization to ensure accurate predictions [45,46]. Figure 2a demonstrates the ANN structure, and Figure 2b shows activation function outputs, which have a range between 1 and 0. The behavior of this function is smooth and S-shaped but not linear.

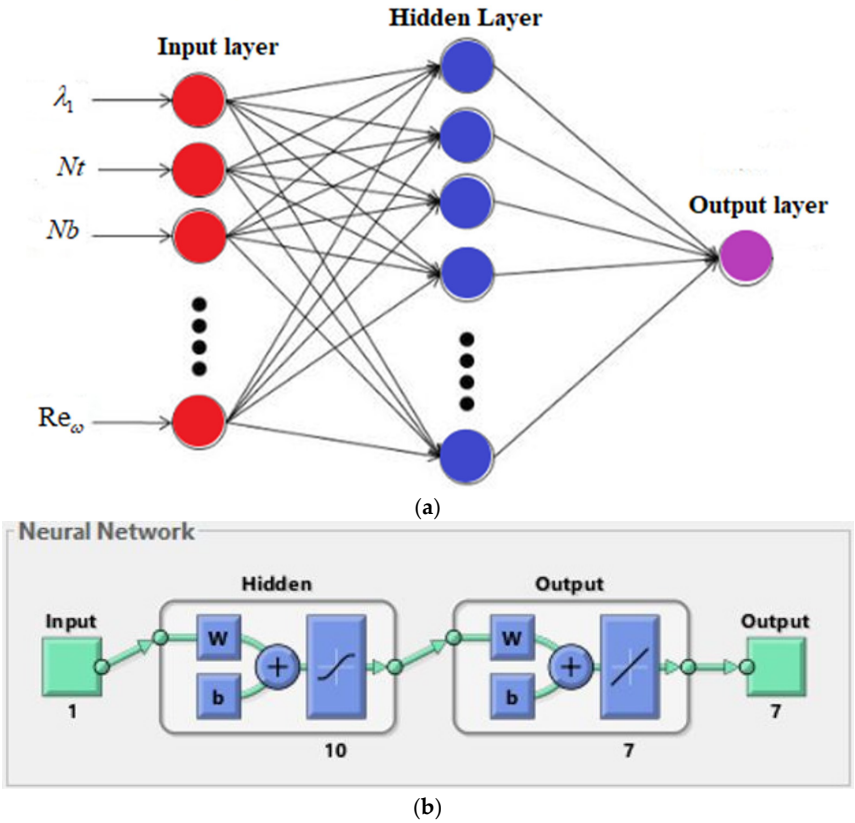

Figure 2. (**a**) ANN structure for model problem. (**b**) ANN design for proposed LMS-NNA.

The researcher chose the Levenberg–Marquardt training algorithm (LMTA) to design the ANN model because it is the most efficient and widely used training method in the literature [47]. The Tan-Sig and Pure lin functions were used for the hidden and output nodes in the design of this ANN [48]. The transfer function, which transforms the loaded dataset into results in the absolute stage of MLPs and BPNNs, is expressed as follows:

$$\widetilde{f}(x) = \frac{1}{1 + \exp(-x)} \tag{17}$$

Improving the network performance is the next challenge for ANN schemes. The functions for the mean squared error (MSE) and the coefficient of determination R-value are expressed as follows:

$$MSE = \frac{1}{n}\sum_{i\geq n}\left(X_{e^i} - X_{ANN(i)}\right)^2, \tag{18}$$

$$R = \sqrt{1 - \frac{\sum_{i\geq n}\left(X_{e^i} - X_{ANN(i)}\right)^2}{\sum_{i\geq n}\left(X_{e^i}\right)^2}}, \tag{19}$$

respectively [49–53]. Moreover, the error rate estimates also contribute to measuring the validness of the ANN design, for which the presumed and intended data are related:

$$\%\ Error\ rate = \left(\frac{X_{\exp} - X_{ANN(i)}}{X_{\exp}}\right) \times 100 \tag{20}$$

4. Analyzing Numerical Results

Figure 3a–e display visual representations of the ANN models. The parameters M and λ have been taken into account to target the fluid velocity $g(\eta)$ in the cone-and-disk system in this scenario. All ANN outcomes are shown in the figures and table. Figure 3a was created to display the MSE for the situation, where $\mathrm{Re}_w = 0$, $\mathrm{Re}_\Omega = 1$ with a fixed disk and a spinning cone, maintaining 1000 epochs with an exceptional authentication representation of 1.6847×10^{-9}. The context of $\mathrm{Re}_w = 0$, $\mathrm{Re}_\Omega = 1$ is explained in detail in Figure 3b, with respect to the 'mu', gradient, and justification. The performance of the first scenario with 20 bins can be compared using the error histogram in Figure 3c. Errors in fitness evaluation graphs for network models are caused by disparities between the reference and target solutions. The current problem's specific curve-fitting statistics are provided in Figure 3d. Evaluating the results of the regression reveals the accuracy of the numerical outcomes. The regression analysis for $\mathrm{Re}_w = 0$, $\mathrm{Re}_\Omega = 1$ is shown in Figure 3e.

Figure 4a–e show how the ANN models perform during training when there are changes in the magnetic factor M versus $g(\eta)$. These figures show that 1.3231×10^{-10} at epoch 597 achieves the optimal authentication presentation. The LMS-NNA is depicted in Figure 5a–e to explain $g(\eta)$ against the Jeffrey fluid parameter λ in the scenario where $\mathrm{Re}_w = 1$, $\mathrm{Re}_\Omega = 0$. These figures show that 2.1258×10^{-9} achieved its optimal authentication presentation at epoch 597. The LMS-NNA is depicted in Figure 6a–e, which show $g(\eta)$ versus M for the scenario where $\mathrm{Re}_w = 1$, $\mathrm{Re}_\Omega = 0$. To demonstrate the LMS-NNA, Figure 7a–e were created to explain the velocity $g(\eta)$ against λ for the situation where $\mathrm{Re}_w = 1$, $\mathrm{Re}_\Omega = 2$. It can be seen from these outputs that the substantiation performance 6.2883×10^{-10} was accomplished at epoch 1000.

The LMS-NNA outputs are displayed in Figure 8a–e, showing the $g(\eta)$ and M relation in the case where $\mathrm{Re}_w = 1$, $\mathrm{Re}_\Omega = 2$. This figure explains the differences between $g(\eta)$ and M by examining the MSE performance, transition workout, error estimation, fitting function, and regression outputs. It is clear that 2.2169×10^{-10} achieved the best validation performance at epoch 1000. In Figure 9a–e, the rotation of both devices in opposite directions is depicted in accordance with the LMS-NNA approach for the proposed model. Here, $g(\eta)$ versus λ is analyzed. The analysis considers MSE outcomes, transition analysis, error estimation, the fitting function, and regression outputs. It can be seen from these outputs that 1.8409×10^{-8} achieved its optimal validation performance at epoch 1000. Figure 10a–e show the same idea about the velocity $g(\eta)$ versus magnetic field when the two devices rotate in opposite directions. Figure 11 shows the variations in the Nt, Nb, λ_1 parameters that were used to investigate the heat transfer rate. The thermophoretic parameter Nt, as well as the Brownian motion parameter Nb, increase the heat transfer, while the Jeffrey fluid parameter λ_1 decreases it.

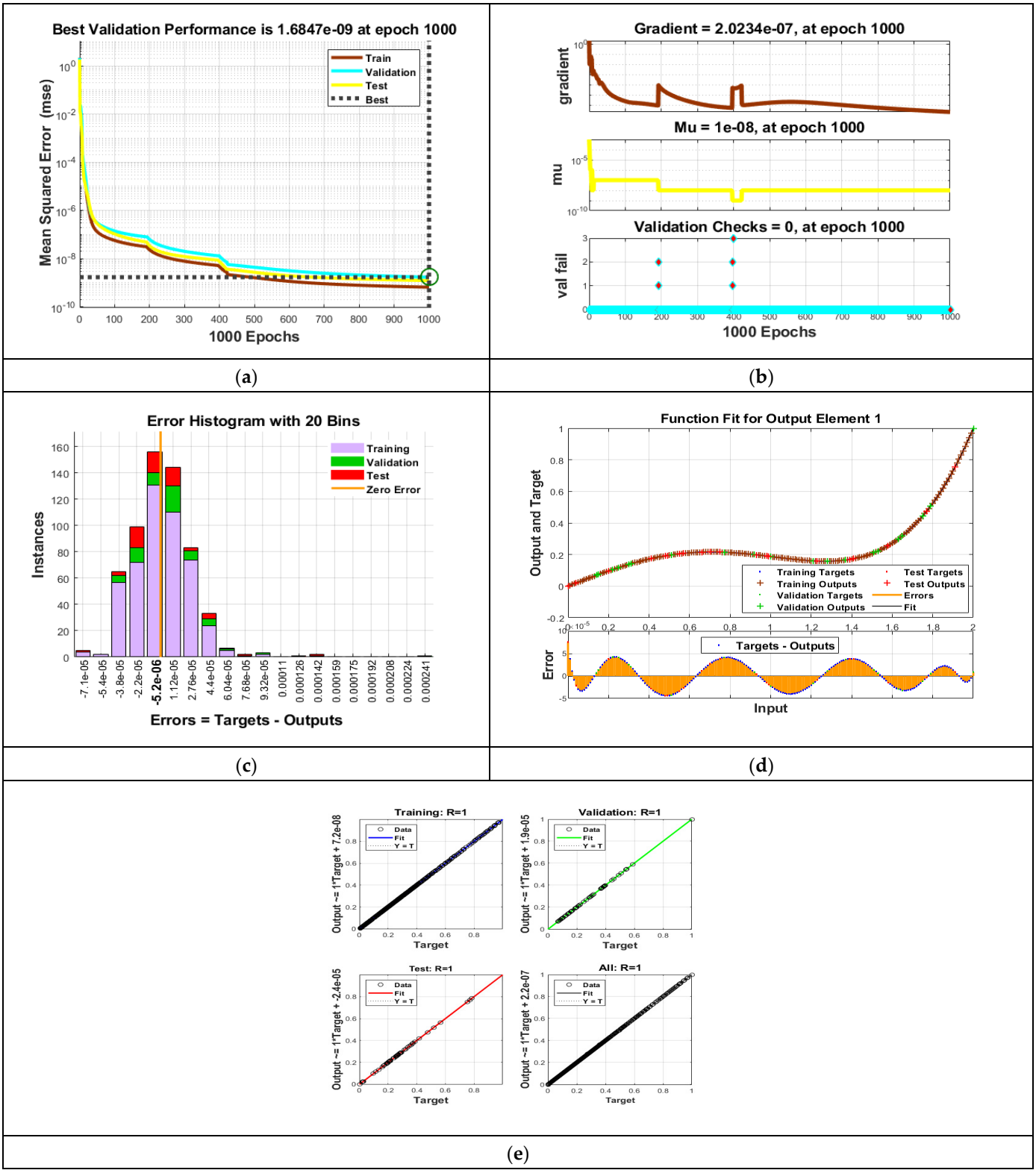

Figure 3. (**a**–**e**) The proposed fluid model $\mathrm{Re}_w = 0$, $\mathrm{Re}_\Omega = 1$ where $g(\eta)$ is plotted using the LMS-NNA for λ.

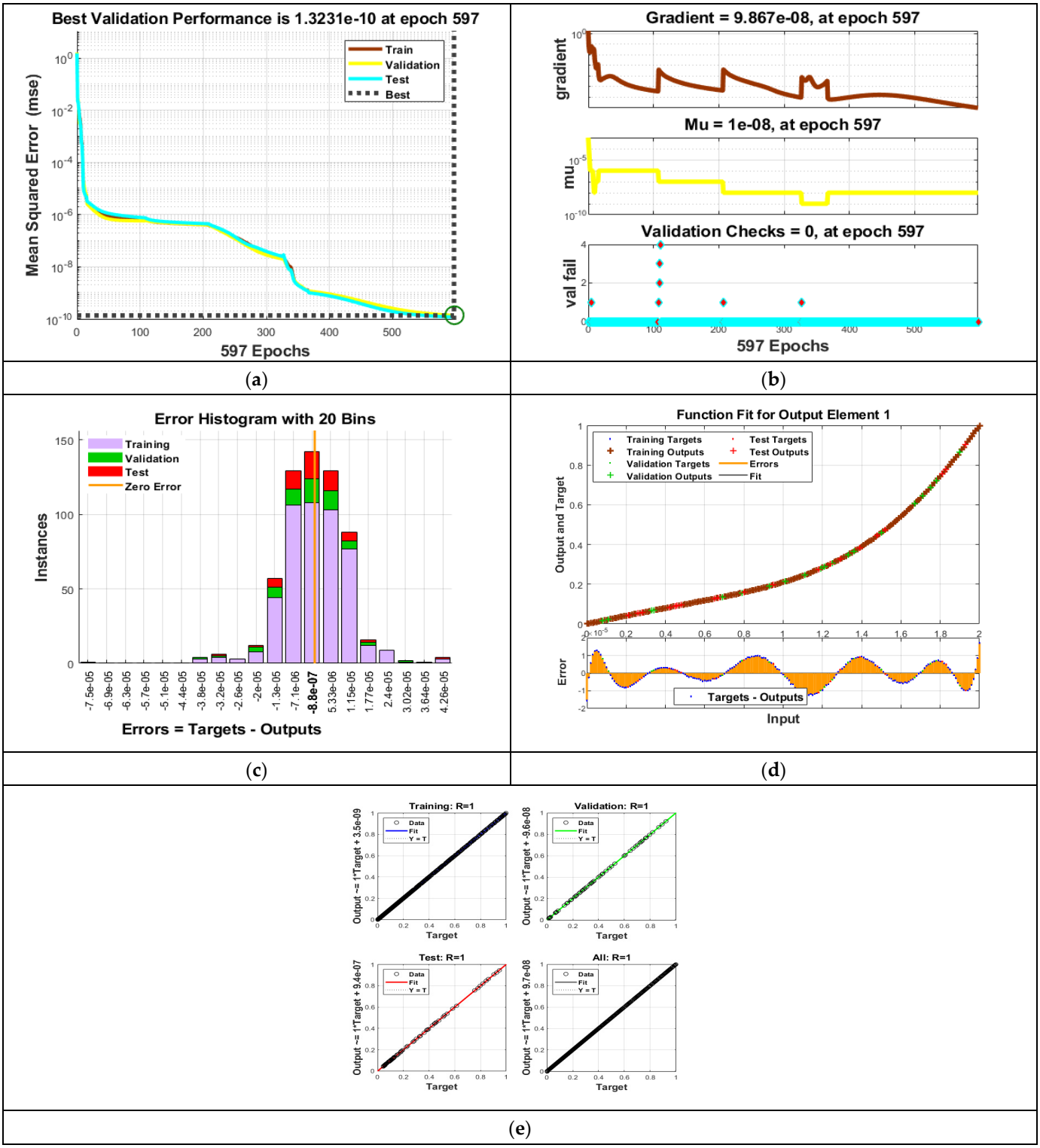

Figure 4. (**a**–**e**) The proposed fluid model $\mathrm{Re}_w = 0$, $\mathrm{Re}_\Omega = 1$; $g(\eta)$ is plotted using the LMS-NNA for M.

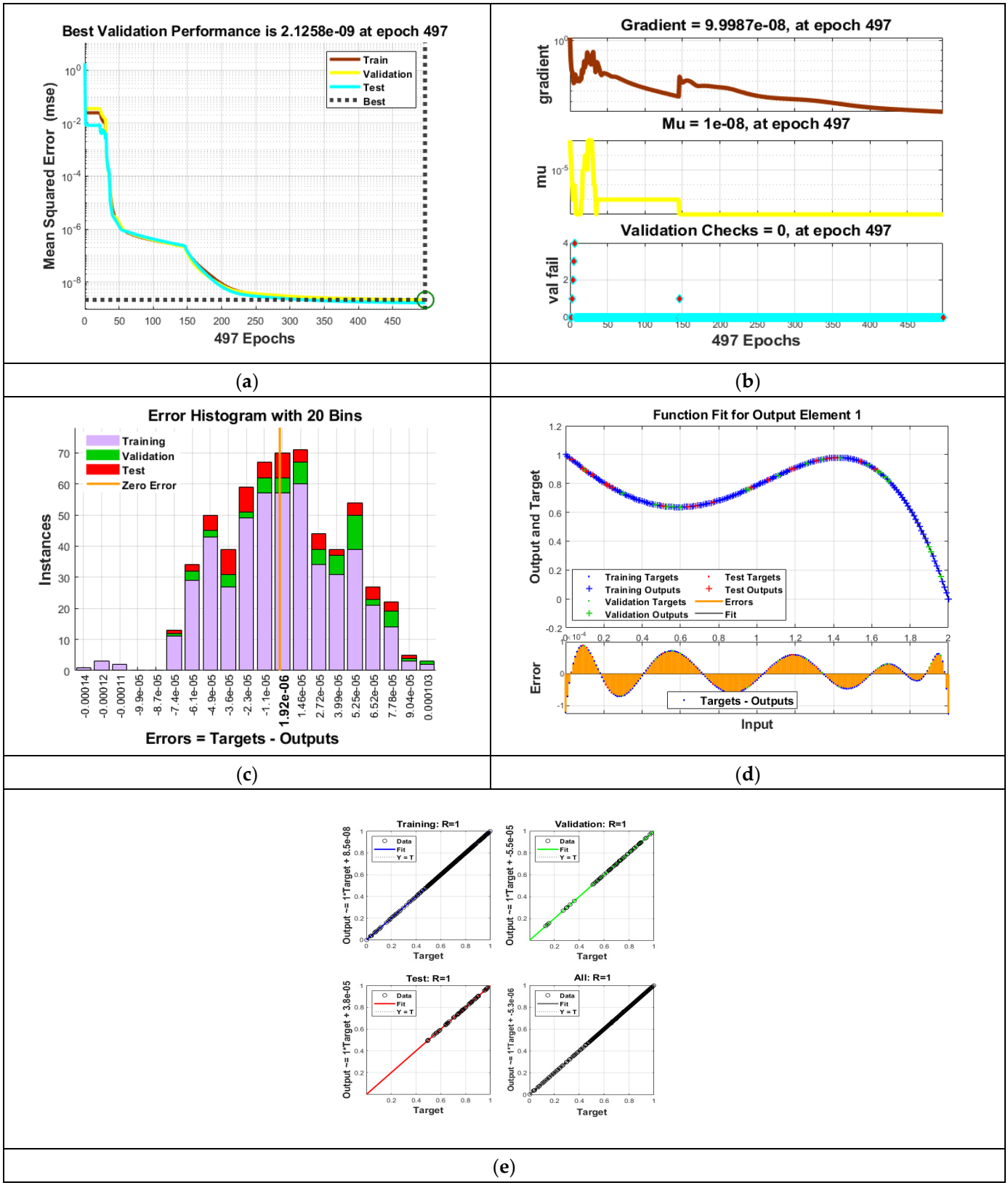

Figure 5. (**a**–**e**) The proposed fluid model $\mathrm{Re}_w = 1$, $\mathrm{Re}_\Omega = 0$; $g(\eta)$ is plotted using the LMS-NNA for λ.

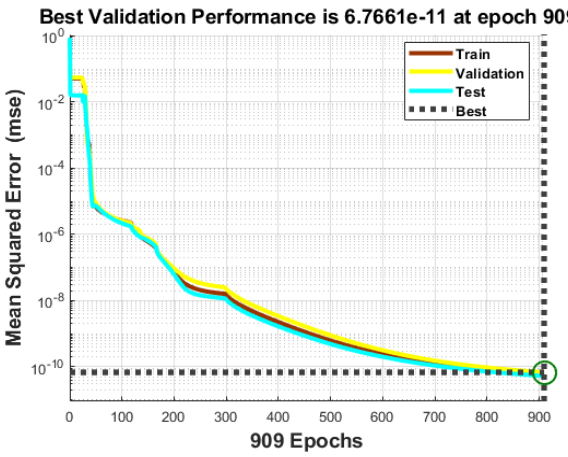

(**a**)

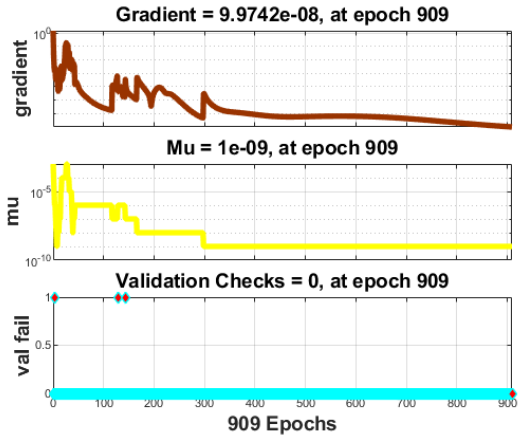

(**b**)

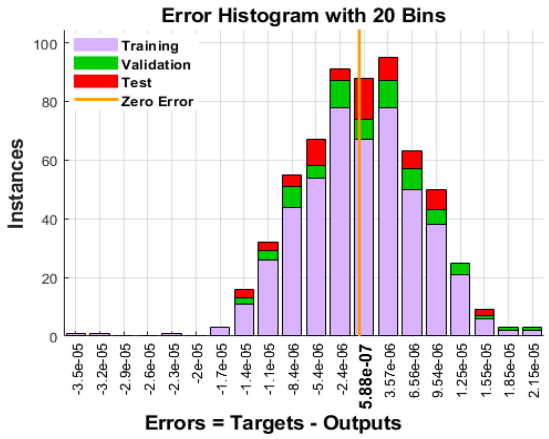

(**c**)

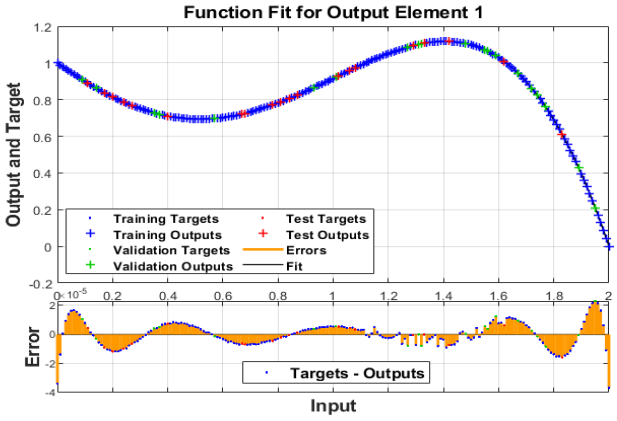

(**d**)

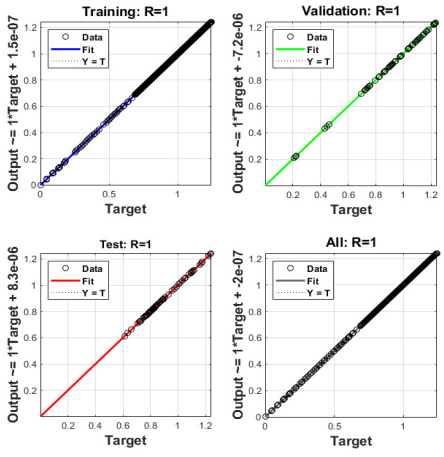

(**e**)

Figure 6. (**a**–**e**) The proposed fluid model $\mathrm{Re}_w = 1$, $\mathrm{Re}_\Omega = 0$; $g(\eta)$ is plotted using the LMS-NNA for M.

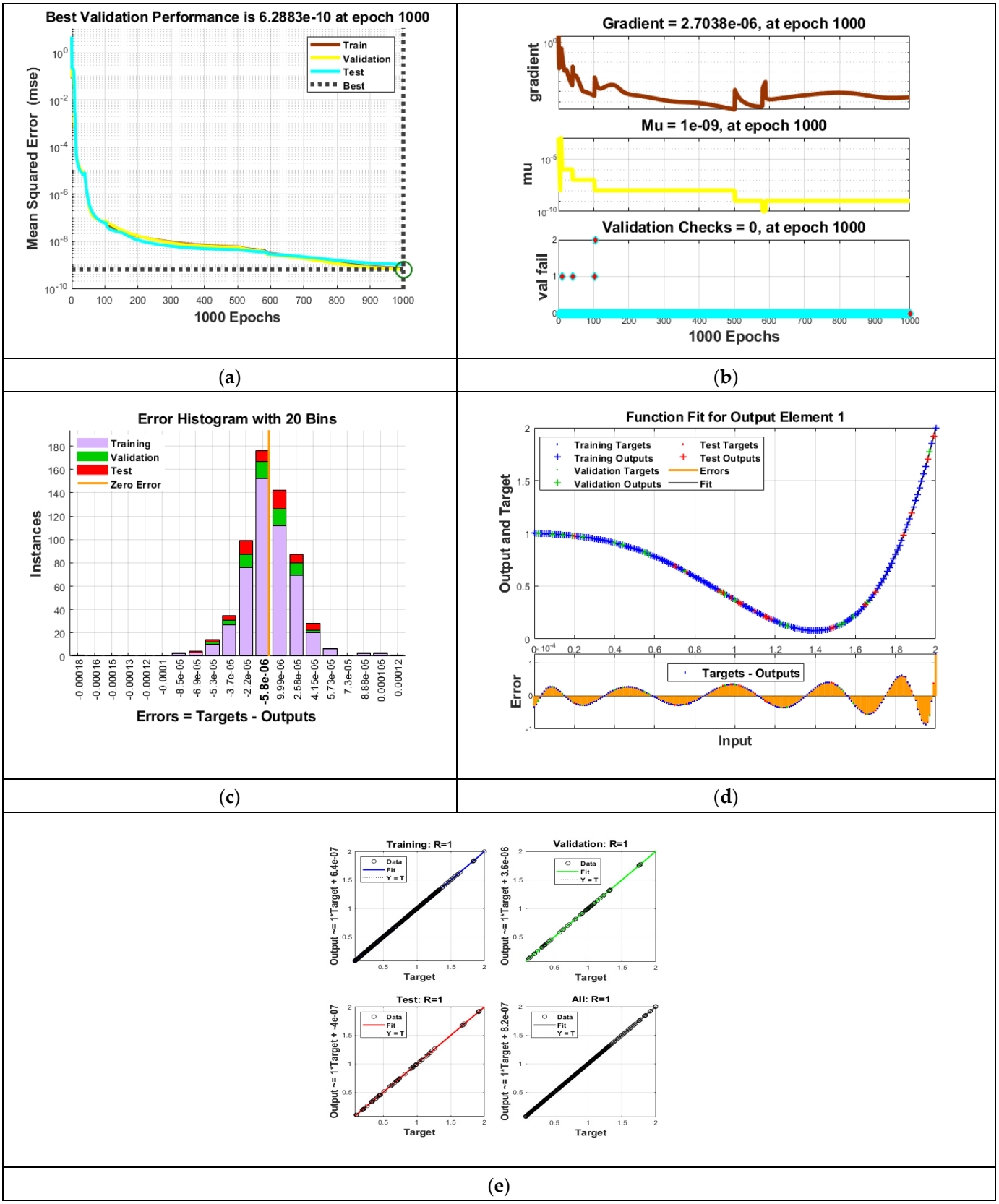

Figure 7. (**a**–**e**) The proposed fluid model $\mathrm{Re}_w = 1,\ \mathrm{Re}_\Omega = 2$; $g(\eta)$ is plotted using the LMS-NNA for λ.

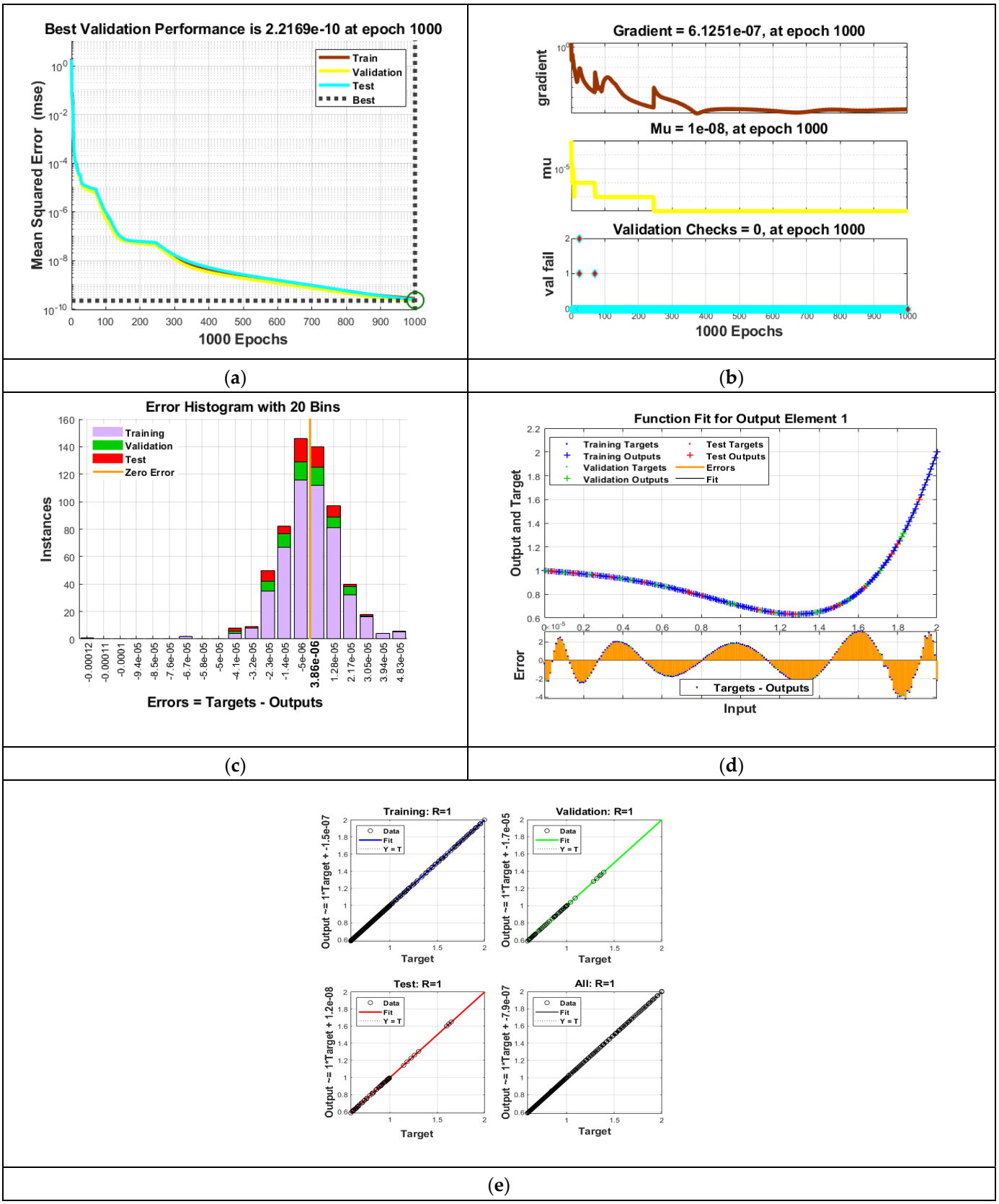

Figure 8. (**a**–**e**) The proposed fluid model $\mathrm{Re}_w = 1$, $\mathrm{Re}_\Omega = 2$ where $g(\eta)$ is plotted using the LMS-NNA for M.

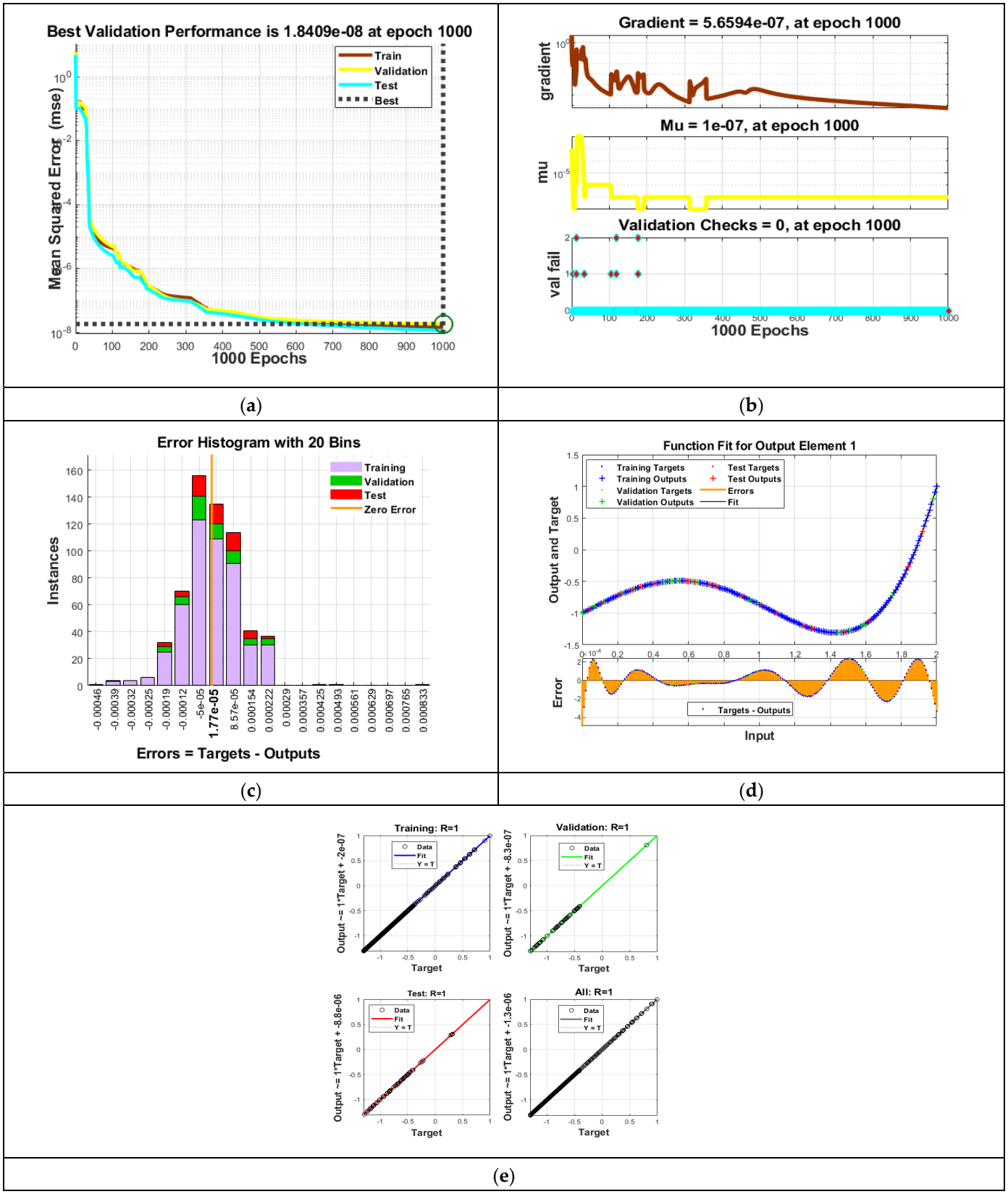

Figure 9. (**a**–**e**) The proposed fluid model $\mathrm{Re}_w = -1$, $\mathrm{Re}_\Omega = 1$ where $g(\eta)$ is plotted using the LMS-NNA for $g(\eta)$.

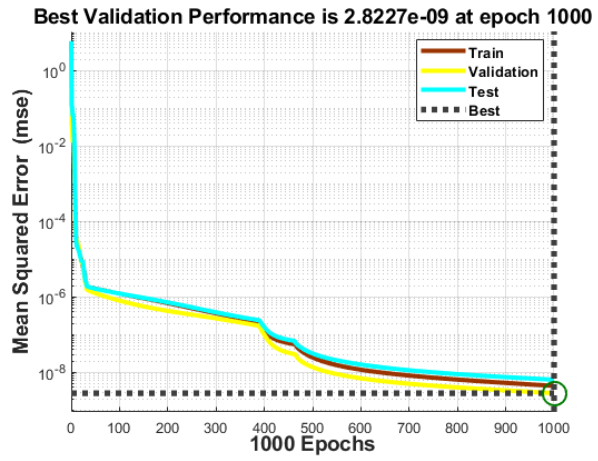

(**a**)

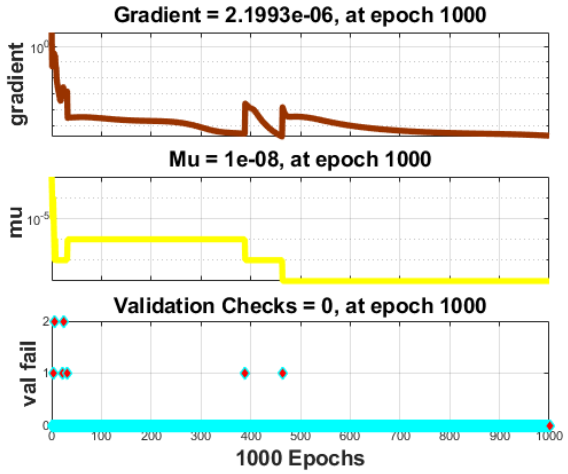

(**b**)

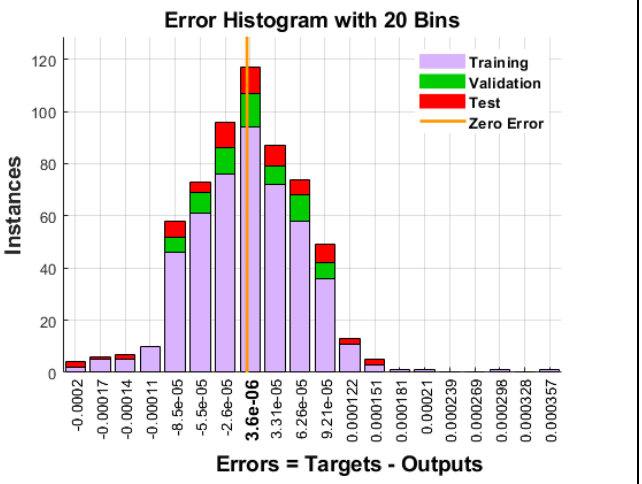

(**c**)

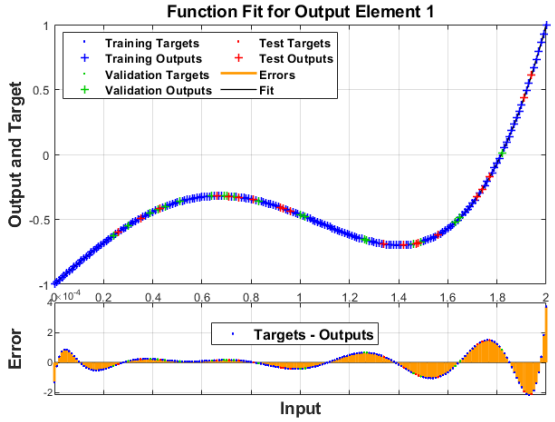

(**d**)

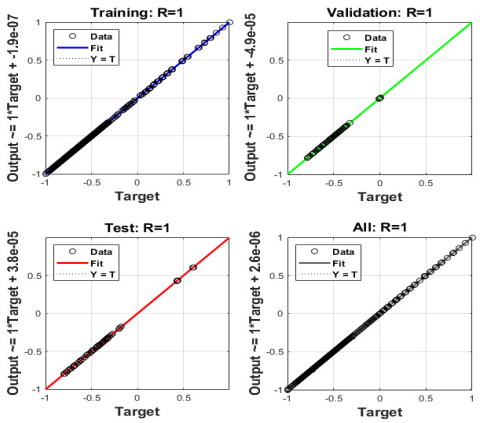

(**e**)

Figure 10. (**a**–**e**) The proposed fluid model $\mathrm{Re}_w = -1$, $\mathrm{Re}_\Omega = 1$ where $g(\eta)$ is plotted using the LMS-NNA for M.

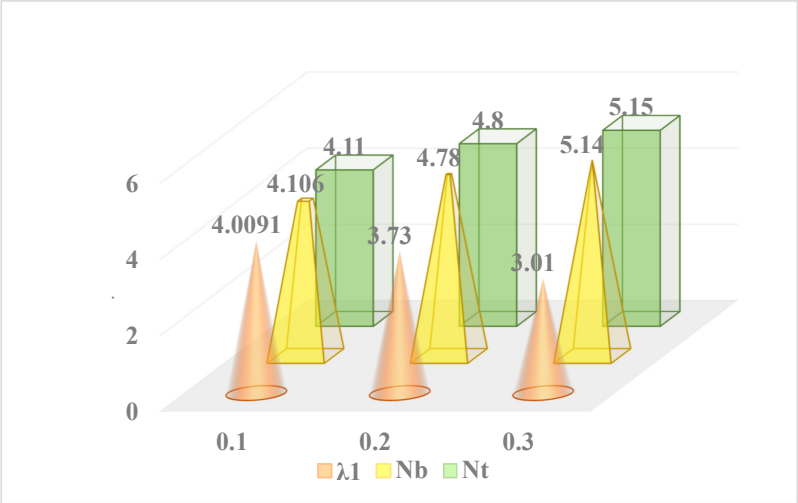

Figure 11. The variation in the heat transfer rate using $Nt, Nb, \lambda 1$.

The velocity term $g(\eta)$ is used in obtaining MSE results, transition analysis, error estimation, the function of fitting, and regression analysis. Table 1 lists the computational values for the ANN models, including the MSE, performance, gradient, and mu values, across different epochs, considering the four different cases. In these cases, the cone is at rest and the disk rotates, the cone rotates and the disk is static, and the disk and cone rotate in either the same or opposite directions. A validation of the present work is demonstrated in Table 2. A very close agreement was reached after considering the four possible cases of cone and disk rotation.

Table 1. Outcomes of the proposed model using the ANN strategy.

Cases	MSE			Performance	Gradient	Mu	Epoch
	Training	Validation	Testing				
1	3.24×10^{-10}	3.67×10^{-9}	2.453×10^{-9}	1.1×10^{-10}	1.2×10^{-7}	10^{-7}	1000
2	2.43×10^{-10}	4.32×10^{-10}	2.34×10^{-10}	2.3×10^{-10}	8.5×10^{-8}	10^{-7}	597
3	3.5×10^{-9}	5.64×10^{-9}	3.2×10^{-9}	3.4×10^{-9}	2.4×10^{-7}	10^{-7}	497
4	4.67×10^{-11}	1.34×10^{-11}	4.65×10^{-11}	3.21×10^{-11}	4.6×10^{-8}	10^{-8}	909
5	4.31×10^{-10}	4.32×10^{-10}	2.45×10^{-9}	3.5×10^{-10}	5.4×10^{-6}	10^{-8}	1000
6	2.54×10^{-10}	1.32×10^{-10}	3.67×10^{-10}	3.6×10^{-10}	3.4×10^{-7}	10^{-7}	1000
7	3.68×10^{-8}	2.45×10^{-8}	2.56×10^{-8}	4.5×10^{-8}	2.1×10^{-7}	10^{-6}	1000
8	2.165×10^{-9}	3.24×10^{-9}	2.43×10^{-9}	1.5×10^{-9}	1.7×10^{-6}	10^{-7}	1000

Table 2. A comparison of the present work with the existing literature, considering common factors.

		Mustafa [3]		Gul et al. [4]		Current Outputs	
Four Models	$\mathbf{Re_\Omega}$, $\mathbf{Re_w}$,	$\Theta'(0)$	$\Theta'(\eta_0)$	$\Theta'(0)$	$\Theta'(\eta_0)$	$\Theta'(0)$	$\Theta'(\eta_0)$
1	$\mathrm{Re}_\Omega = 1,$ $\mathrm{Re}_w = 0,$	4.376528	5.276516	4.376427	5.276632	4.376431	5.276671
2	$\mathrm{Re}_\Omega = 0,$ $\mathrm{Re}_w = 1,$	4.1862734	5.162854	4.1863266	5.162923	4.186356	5.162952
3	$\mathrm{Re}_\Omega = 1,$ $\mathrm{Re}_w = 1,$	3.7235190	4.328610	3.7236278	4.328723	3.723687	4.328742
4	$\mathrm{Re}_\Omega = -1,$ $\mathrm{Re}_w = 1,$	5.2532413	6.024516	5.2533256	6.024627	5.253372	6.024661

For the four salient cases, i.e., (i) $\mathrm{Re}_\Omega > 0$, $\mathrm{Re}_w = 0$, (ii) $\mathrm{Re}_\Omega = 0$, $\mathrm{Re}_w > 0$, (iii) $\mathrm{Re}_\Omega > 0$, $\mathrm{Re}_w > 0$, and (iv) $\mathrm{Re}_w < 0$, $\mathrm{Re}_\Omega > 0$, taken into consideration, the behaviors of the transverse component of the velocity field through the cone–disk space against the preceding Jeffrey fluid parameter λ and magnetic parameter M are examined. The effects of the earlier factors are plotted in Figures 12a, 13a, 14a, and 15a, while the latter are depicted in Figures 16a, 17a, 18a, and 19a, respectively. The impacts regarding $g(\eta)$ in response to increases in λ and M, in a situation where the cone is still and the disk rotates uniformly ((i) $\mathrm{Re}_w = 0$, $\mathrm{Re}_\Omega = 1$), can be seen in Figures 12a and 16a, respectively. Figure 12a portrays the declining aspects of λ. It is worth mentioning that the Jeffrey fluid factor usually quantifies the non-Newtonian rheology of fluids, which, when discussing the transverse velocity $g(\eta)$, measures the resistance offered in response to shear stresses.

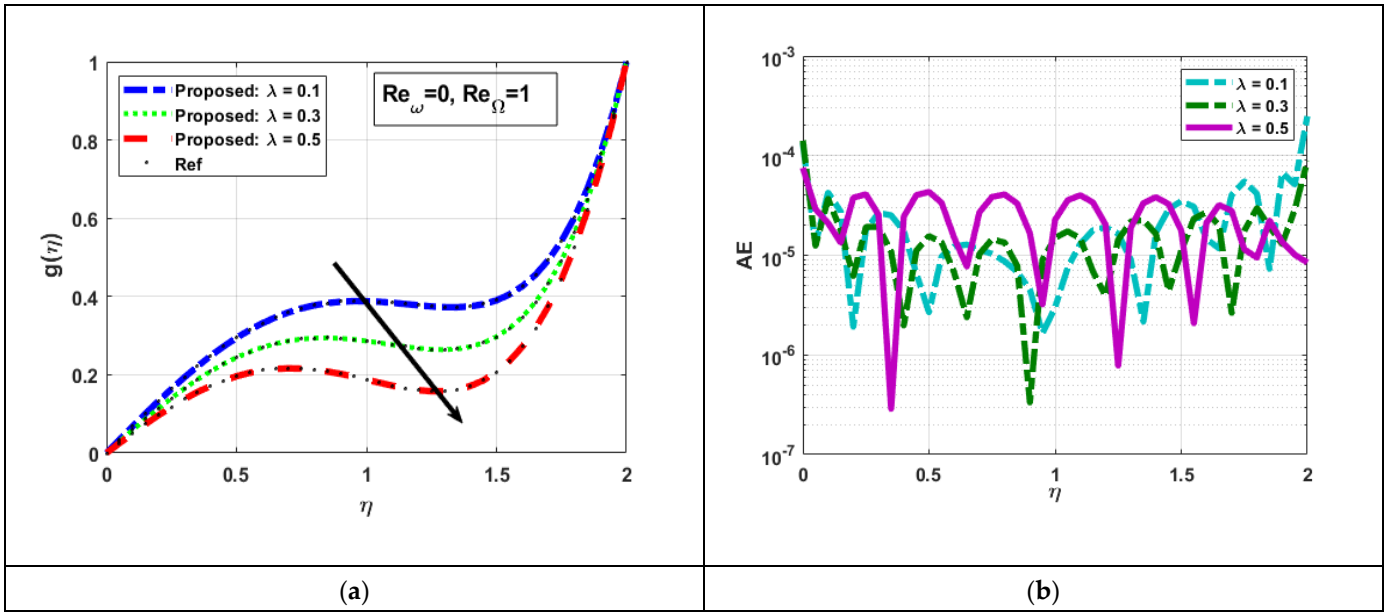

(**a**) (**b**)

Figure 12. (**a**) Disparity in λ vs. $g(\eta)$; (**b**) λ vs. AE.

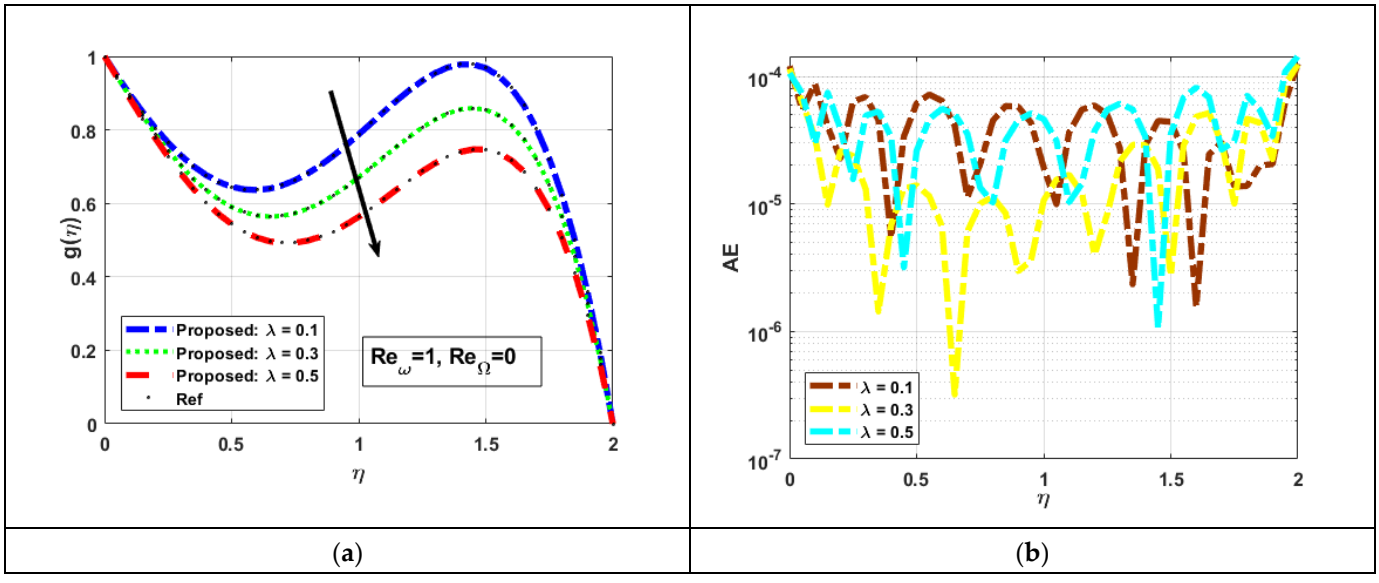

(**a**) (**b**)

Figure 13. (**a**) Disparity in λ & $g(\eta)$; (**b**) λ vs. AE.

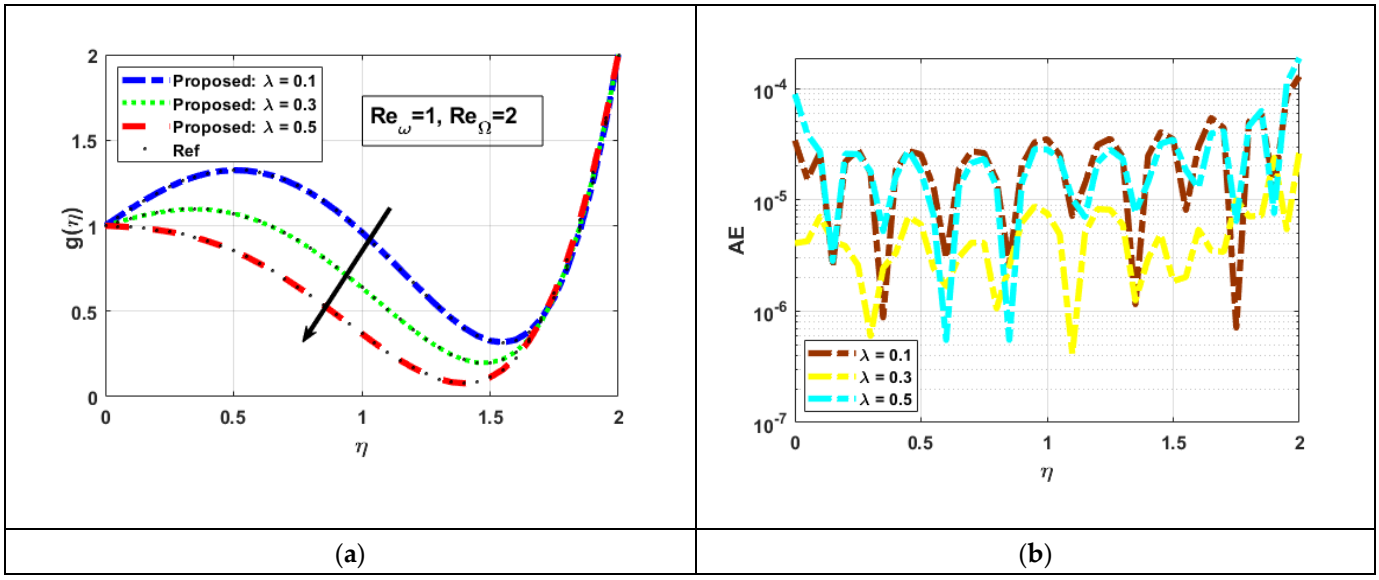

Figure 14. (**a**) Disparity in λ & $g(\eta)$; (**b**) λ vs. AE.

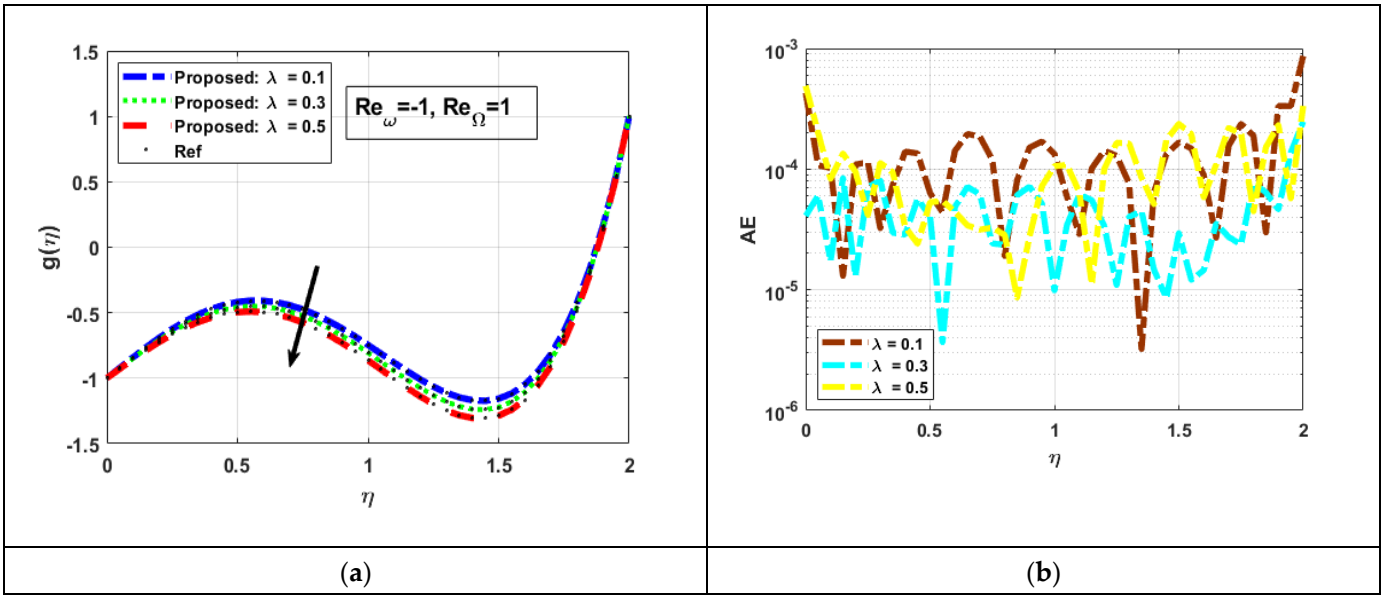

Figure 15. (**a**) Disparity in λ & $g(\eta)$; (**b**) λ vs. AE.

This implies that a higher range of λ is unfavorable for the deformation of the media, offering a higher resistance to the flow rate in the transverse direction. Put another way, the fluid becomes more vicious and, thus, limits the rate $g(\eta)$ as λ increases. This explanation is the basis for Figure 12a. Moreover, the adverse tendency of M in the context of $g(\eta)$ can be clearly seen in Figure 16a. This behavior can be elaborated via the reinforced and tempered magnetic field through the flow expanse. Magnetic effects are responsible for inducing normal-oriented Lorentz forces, which, in turn, restrict streaming along the transverse orientation. Henceforth, increments in M strengthen these restraining sources while compelling the fluid molecules to line up alongside the magnetic field lines. This, contrary to axial regulations, discourages the advection of the fluidic streams in transverse directions and, consequently, causes $g(\eta)$ to decrease throughout the canonical gap. Likewise, the resistant nature of the Jeffrey fluidic material and magnetic source results in adverse outcomes regarding the transverse flow rate in the resting ternary situations, i.e., (ii) $\mathrm{Re}_\Omega = 0,\ \mathrm{Re}_w = 1$, (iii) $\mathrm{Re}_\Omega = 2,\ \mathrm{Re}_w = 1$, and (iv) $\mathrm{Re}_\Omega = 1,\ \mathrm{Re}_w = -1$. Figures 13a, 14a and 15a portray the

declining aspects of $g(\eta)$ in response to increases in λ, while the decreasing impacts of M on $g(\eta)$ can be seen in Figures 17a, 18a and 19a sequentially. Part (b) of all Figures 12–19 shows how to analyze the absolute error (AE) in ANN (artificial neural network) models to verify their conformity to correctness criteria. Each model's calculated absolute error values are positioned within the specific predefined ranges of 10^{-7}–10^{-3} and 10^{-8}–10^{-4} for their respective ANN configurations. These numerical error results show the commendable level of accuracy found in the considered ANN models, demonstrating their strength and consistency when compared to the reference results.

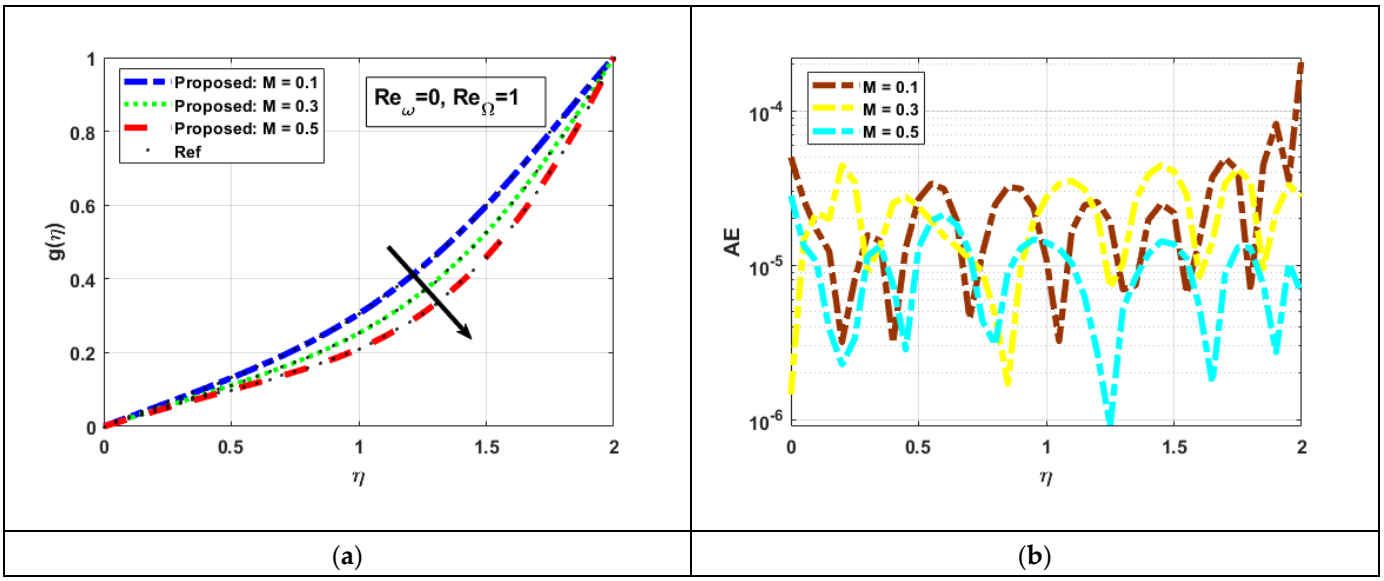

(**a**) (**b**)

Figure 16. (**a**) Disparity in M & $g(\eta)$; (**b**) M vs. AE.

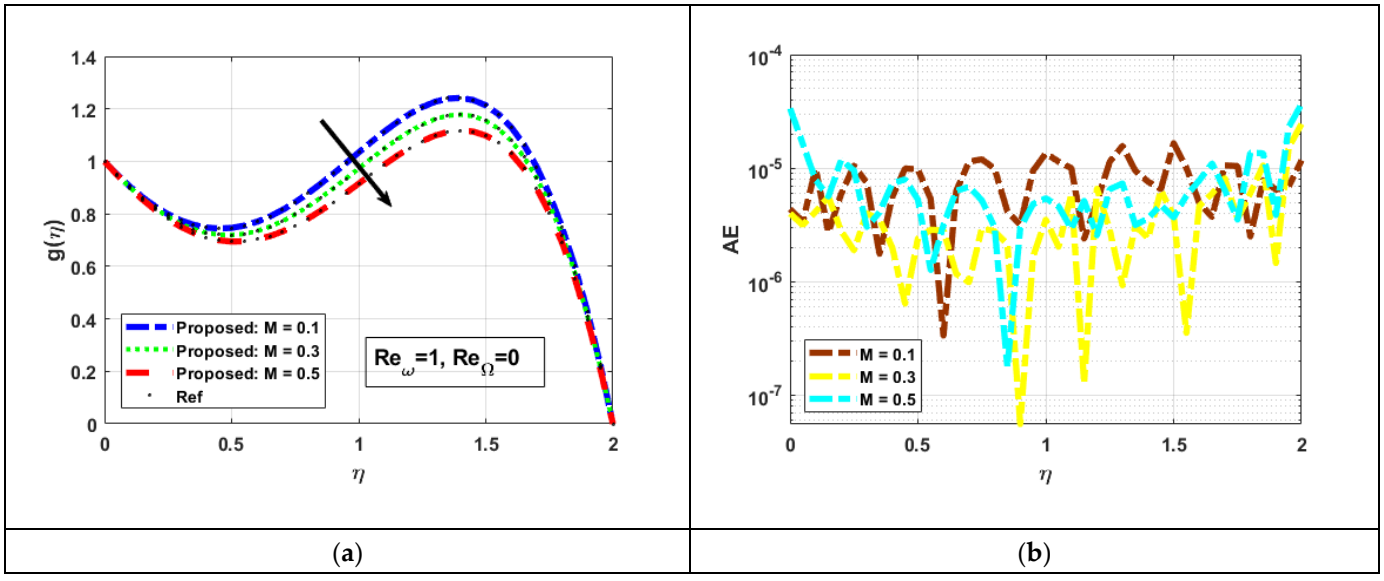

(**a**) (**b**)

Figure 17. (**a**) Disparity in M & $g(\eta)$; (**b**) M vs. AE.

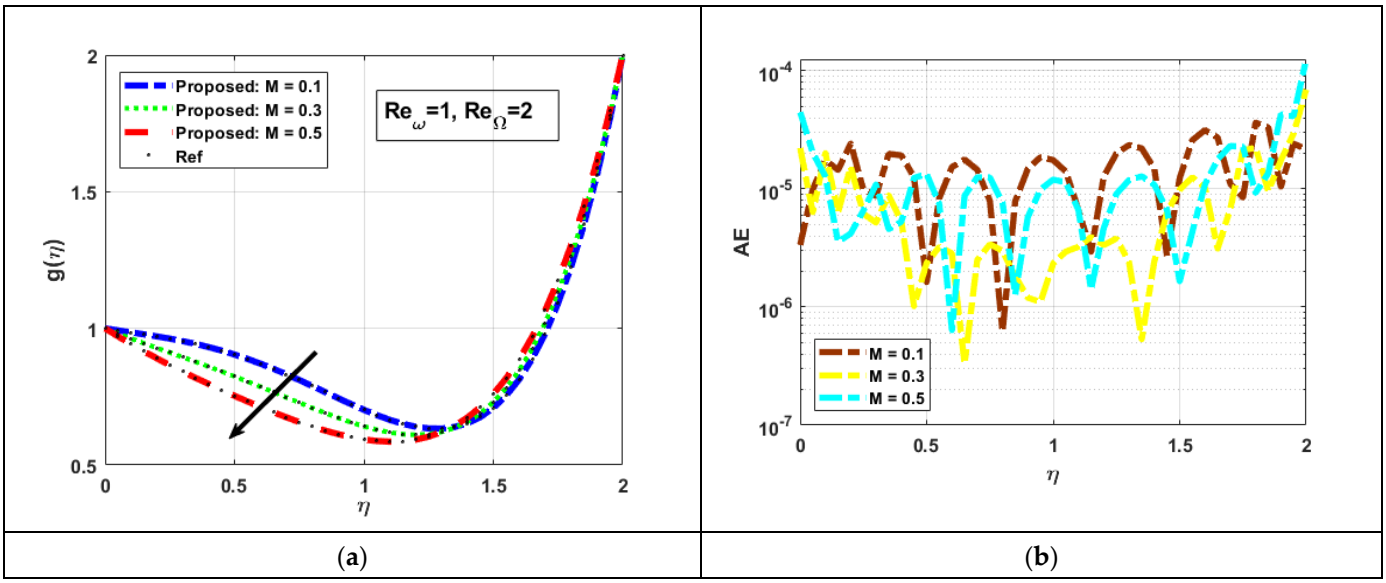

Figure 18. (**a**) Disparity in M & $g(\eta)$; (**b**) M vs. AE.

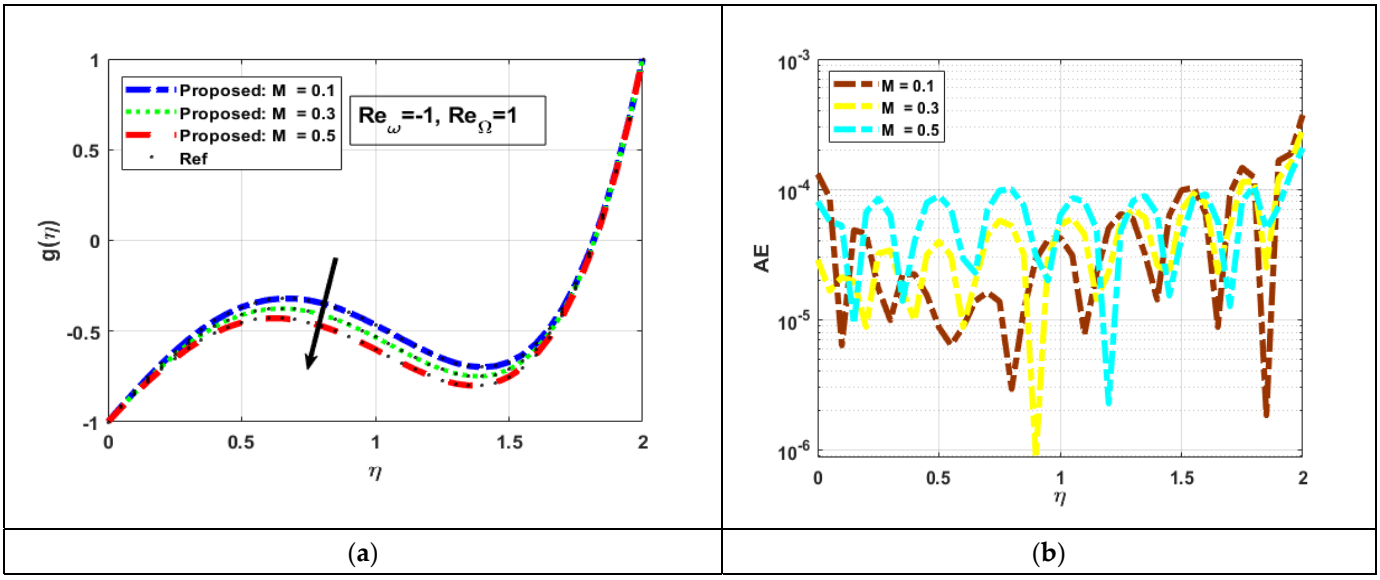

Figure 19. (**a**) Disparity in M & $g(\eta)$; (**b**) M vs. AE.

5. Conclusions

The Boungiorno description is utilized in this study to analyze the streaming of a viscoelastic fluid within the gap of a cone–disk configuration. The supervising model is transformed into a nonlinear system of ordinary differential equations, which is then handled using a neurocomputational technique to assess its solution. Four distinct scenarios are investigated to examine the effects of the simultaneous motion of the cone and disk on fluid flow, with one component rotating while the other is held at rest, i.e., (i) a spinning disk and stationary cone or (ii) vice versa, and by having the components co-rotate in (iii) parallel or (iv) opposite directions. The optimized stimulations and outcomes regarding the considered flow problem are assessed using an artificial neural network (ANN). Its effectiveness is demonstrated via the results of our study, summarizing the potential to revolutionize fluid flow control across a wide range of engineering fields. Meanwhile, by using coupling processes like training, testing, and validation in reference to the sampling datasets, the design methodology successfully employs a structured sequence to address

various aspects of the transfer rates. The execution efficiency of the least mean square neural network algorithm (LMS-NNA) is investigated by incorporating various statistical aids, i.e., the mean square error (MSE), regressive graphs, uncertainty histograms, and curve-fitting plots. This analysis of the fluid stream problem leads to the following key points and conclusions:

- The non-Newtonian behavior of Jeffery fluids enhances the heat transfer rate, leading to improved efficiency in heat-exchanger systems.
- The food-processing industry uses Jeffrey fluids to control the heating and cooling of various food products.
- The present work is validated with the existing literature, as shown in Table 2. Four possible cases of cone and disk rotation are considered, and very close agreement is obtained.
- Training, testing and analysis, and authentication were achieved for the velocity field, temperature distribution, and concentration profile. On average, these equations exhibited a close configuration and settlement consistent with these results at 10^{-8}.
- The LMS-NNA's exceptional accuracy is demonstrated through the fact that the estimated error (AE) between the reference and targeted data falls within the range of 10^{-4} to 10^{-5}.

Future work: The current work is extendable to other non-Newtonian fluids, including Oldroyed B fluids, Williamson fluids, and Carreau–Yasuda fluids. Experimental analysis using this theoretical approach will be very helpful in mechanical engineering.

Funding: This research received no external funding.

Data Availability Statement: The data that support the findings of this study are available upon reasonable request from the corresponding author.

Conflicts of Interest: The author declares no conflicts of interest.

References

1. Khadrawi, A.F.; Al-Nimr, M.A.; Othman, A. The Jeffreys model is a good way to understand basic viscoelastic fluid flow problems. *Chem. Eng. Sci.* **2005**, *60*, 7131–7136. [CrossRef]
2. Hayat, T.; Ali, N.; Asghar, S. The flow of a Jeffrey fluid is analyzed by peristaltic transport. *Acta Mech.* **2007**, *193*, 101–112. [CrossRef]
3. Wang, F.; Rani, S.P.; Sarada, K.; Gowda, R.P.; Zahran, H.Y.; Mahmoud, E.E. The effects of nanoparticle aggregation and radiation on the flow of nanofluid between the gap of a disk and cone. *Case Stud. Therm. Eng.* **2022**, *33*, 101930. [CrossRef]
4. Moatimid, G.M.; Mohamed, M.A.; Elagamy, K. A Casson nanofluid flow within the conical gap between rotating surfaces of a cone and a horizontal disc. *Sci. Rep.* **2022**, *12*, 11275. [CrossRef] [PubMed]
5. Turkyilmazoglu, M. On the fluid flow and heat transfer between a cone and a disk both stationary or rotating. *Math. Comput. Simul.* **2020**, *177*, 329–340. [CrossRef]
6. Gul, T.; Kashifullah Bilal, M.; Alghamdi, W.; Asjad, M.I.; Abdeljawad, T. Hybrid nanofluid flow within the conical gap between the cone and the surface of a rotating disk. *Sci. Rep.* **2021**, *11*, 1180. [CrossRef]
7. Srilatha, P.; Remidi, S.; Nagapavani, M.; Singh, H.; Prasannakumara, B.C. Heat and mass transfer analysis of a fluid flow across the conical gap of a cone-disk apparatus under the thermophoretic particles motion. *Energies* **2023**, *16*, 952. [CrossRef]
8. Shevchuk, I.V. An improved asymptotic expansion method for fluid flow and convective heat transfer in cone-and-disk geometries with rotating cone. *Phys. Fluids* **2023**, *35*, 043603. [CrossRef]
9. Maraj, E.N.; Akbar, N.S.; Kousar, N.; Zehra, I.; Muhammad, T. Thermal enhancement of nano-fluidic transport confined between disk and cone both rotating with distinct angular velocities and heat transfer. *Int. J. Numer. Methods Heat Fluid Flow* **2023**, *34*, 473–493. [CrossRef]
10. Basavarajappa, M.; Bhatta, D. Lie group analysis of flow and heat transfer of a nanofluid in cone–disk systems with Hall current and radiative heat flux. *Math. Methods Appl. Sci.* **2023**, *46*, 15838–15867. [CrossRef]
11. Nazeer, M.; Hussain, F.; Ahmad, M.O.; Saeed, S.; Khan, M.I.; Kadry, S.; Chu, Y.M. Multi-phase flow of Jeffrey fluid bounded within magnetized horizontal surface. *Surf. Interfaces* **2021**, *22*, 100846. [CrossRef]
12. Tanuja, T.N.; Kavitha, L.; Ur Rehman, K.; Shatanawi, W.; Varma, S.V.K.; Kumar, G.V. Heat transfer in magnetohydrodynamic Jeffery–Hamel molybdenum disulfide/water hybrid nanofluid flow with thermal radiation: A neural networking analysis. *Numer. Heat Transf. Part A Appl.* **2024**, 1–19. [CrossRef]
13. Sharma, B.K.; Kumar, A.; Gandhi, R.; Bhatti, M.M. Exponential space and thermal-dependent heat source effects on electro-magneto-hydrodynamic Jeffrey fluid flow over a vertical stretching surface. *Int. J. Mod. Phys. B* **2022**, *36*, 2250220. [CrossRef]

14. Sharma, B.K.; Sharma, P.; Mishra, N.K.; Noeiaghdam, S.; Fernandez-Gamiz, U. Bayesian regularization networks for micropolar ternary hybrid nanofluid flow of blood with homogeneous and heterogeneous reactions: Entropy generation optimization. *Alex. Eng. J.* **2023**, *77*, 127–148. [CrossRef]
15. Agarwal, V.; Singh, B.; Nisar, K.S. Numerical analysis of heat transfer in magnetohydrodynamic micropolar Jeffery fluid flow through porous medium over a stretching sheet with thermal radiation. *J. Therm. Anal. Calorim.* **2022**, *147*, 9829–9851. [CrossRef]
16. Benal, S.S.; Tawade, J.V.; Biradar, M.M.; Allasi, H.L. Effects of the magnetohydrodynamic flow within the boundary layer of a jeffery fluid in a porous medium over a shrinking/stretching sheet. *Math. Probl. Eng.* **2022**, *2022*, 7326504. [CrossRef]
17. Rasool, G.; Zhang, T.; Shafiq, A. Second grade nanofluidic flow past a convectively heated vertical Riga plate. *Phys. Scr.* **2019**, *94*, 125212. [CrossRef]
18. Shafiq, A.; Sindhu, T.N.; Khalique, C.M. Numerical investigation and sensitivity analysis on bioconvective tangent hyperbolic nanofluid flow towards stretching surface by response surface methodology. *Alex. Eng. J.* **2020**, *59*, 4533–4548. [CrossRef]
19. Shafiq, A.; Mebarek-Oudina, F.; Sindhu, T.N.; Abidi, A. A study of dual stratification on stagnation point Walters' B nanofluid flow via radiative Riga plate: A statistical approach. *Eur. Phys. J. Plus* **2021**, *136*, 407. [CrossRef]
20. Kukreja, H.; Bharath, N.; Siddesh, C.S.; Kuldeep, S. An introduction to artificial neural network. *Int. J. Adv. Res. Innov. Ideas Educ.* **2016**, *1*, 27–30.
21. Morimoto, M.; Fukami, K.; Zhang, K.; Fukagata, K. Generalization techniques of neural networks for fluid flow estimation. *Neural Comput. Appl.* **2022**, *34*, 3647–3669. [CrossRef]
22. Li, A.; Yuen, A.C.Y.; Wang, W.; Chen, T.B.Y.; Lai, C.S.; Yang, W.; Wu, W.; Chan, Q.N.; Kook, S.; Yeoh, G.H. Integration of computational fluid dynamics and artificial neural network for optimization design of battery thermal management system. *Batteries* **2022**, *8*, 69. [CrossRef]
23. Affonso, R.R.; Dam, R.S.; Salgado, W.L.; da Silva, A.X.; Salgado, C.M. Flow regime and volume fraction identification using nuclear techniques, artificial neural networks and computational fluid dynamics. *Appl. Radiat. Isot.* **2020**, *159*, 109103. [CrossRef] [PubMed]
24. Mulashani, A.K.; Shen, C.; Nkurlu, B.M.; Mkono, C.N.; Kawamala, M. Enhanced group method of data handling (GMDH) for permeability prediction based on the modified Levenberg Marquardt technique from well log data. *Energy* **2022**, *239*, 121915. [CrossRef]
25. Lv, C.; Xing, Y.; Zhang, J.; Na, X.; Li, Y.; Liu, T.; Wang, F.Y. Levenberg–Marquardt backpropagation training of multilayer neural networks for state estimation of a safety-critical cyber-physical system. *IEEE Trans. Ind. Inform.* **2017**, *14*, 3436–3446. [CrossRef]
26. Jegan, J.; Suresh, R.; Subramanian, E.K.; Ramachandran, A.; Reddy, S.R.R.; Jakeer, S. Analysis of Numerical Computation and ANN Modelling on the Bio-Magnetic Darcy-Forchheimer Ternary Hybrid Nanofluid Flow: Entropy Generation. *BioNanoScience* **2024**, *14*, 2602–2624. [CrossRef]
27. Sharma, B.K.; Sharma, P.; Mishra, N.K.; Fernandez-Gamiz, U. Darcy-Forchheimer hybrid nanofluid flow over the rotating Riga disk in the presence of chemical reaction: Artificial neural network approach. *Alex. Eng. J.* **2023**, *76*, 101–130. [CrossRef]
28. Ullah, H.; Alqahtani, A.M.; Raja, M.A.Z.; Fiza, M.; Ullah, K.; Omer, A.S.; Khan, I.; Shoaib, M. Numerical treatment based on artificial neural network to Soret and Dufour effects on MHD squeezing flow of Jeffrey fluid in horizontal channel with thermal radiation. *Int. J. Thermofluids* **2024**, *23*, 100725. [CrossRef]
29. Sulaiman, M.; Khan, N.A.; Alshammari, F.S.; Laouini, G. Performance of heat transfer in micropolar fluid with isothermal and isoflux boundary conditions using supervised neural networks. *Mathematics* **2023**, *11*, 1173. [CrossRef]
30. Sharma, B.K.; Khanduri, U.; Mishra, N.K.; Mekheimer, K.S. Combined effect of thermophoresis and Brownian motion on MHD mixed convective flow over an inclined stretching surface with radiation and chemical reaction. *Int. J. Mod. Phys. B* **2023**, *37*, 2350095. [CrossRef]
31. Rashid, A.; Dawar, A.; Ayaz, M.; Islam, S.; Galal, A.M.; Gul, H. Homotopic solution of the chemically reactive magnetohydrodynamic flow of a hybrid nanofluid over a rotating disk with Brownian motion and thermophoresis effects. *ZAMM-J. Appl. Math. Mech./Z. Angew. Math. Mech.* **2023**, *103*, e202200262. [CrossRef]
32. Khan, A.; Iqbal, Z.; Ahammad, N.A.; Sidi, M.O.; Elattar, S.; Awad, S.; Eldin, S.M. Bioconvection Maxwell nanofluid flow over a stretching cylinder influenced by chemically reactive activation energy surrounded by a permeable medium. *Front. Phys.* **2023**, *10*, 1348. [CrossRef]
33. Janapatla, P.; Chakraborty, A. Mixed convection nanofluid flow using lie group scaling with the impact of MHD radiation thermophoresis and brownian motion. *J. Adv. Res. Fluid Mech. Therm. Sci.* **2023**, *101*, 85–98. [CrossRef]
34. Khoshtarash, H.; Siavashi, M.; Ramezanpour, M.; Blunt, M.J. Pore-scale analysis of two-phase nanofluid flow and heat transfer in open-cell metal foams considering Brownian motion. *Appl. Therm. Eng.* **2023**, *221*, 119847. [CrossRef]
35. Lone, S.A.; Shamshuddin, M.D.; Shahab, S.; Iftikhar, S.; Saeed, A.; Galal, A.M. Computational analysis of MHD driven bioconvective flow of hybrid Casson nanofluid past a permeable exponential stretching sheet with thermophoresis and Brownian motion effects. *J. Magn. Magn. Mater.* **2023**, *580*, 170959. [CrossRef]
36. Majeed, A.; Zeeshan, A.; Jawad, M. Double stratification impact on radiative MHD flow of nanofluid toward a stretchable cylinder under thermophoresis and brownian motion with multiple slip. *Int. J. Mod. Phys. B* **2023**, *37*, 2350232. [CrossRef]
37. Felicita, A.; Venkatesh, P.; Gireesha, B.J.; Krishnamurthy, M.R. Slip and convective flow of Williamson nanofluid influenced by Brownian motion and thermophoresis mechanism in a horizontal microchannel. *Proc. Inst. Mech. Eng. Part N J. Nanomater. Nanoeng. Nanosyst.* **2023**, 23977914231177340. [CrossRef]

38. Ibrahim, S.M.; Kumar, P.V.; Lorenzini, G. Influence of Thermophoresis and Brownian Motion of Nanoparticles on Radiative Chemically-Reacting MHD Hiemenz Flow over a Nonlinear Stretching Sheet with Heat Generation. *Fluid Dyn. Mater. Process.* **2023**, *19*, 855–868. [CrossRef]
39. Almeida, F.; Gireesha, B.J.; Venkatesh, P. Magnetohydrodynamic flow of a micropolar nanofluid in association with Brownian motion and thermophoresis: Irreversibility analysis. *Heat Transf.* **2023**, *52*, 2032–2055. [CrossRef]
40. Gul, T.; Ahmed, Z.; Jawad, M.; Saeed, A.; Alghamdi, W. Bio-convectional nanofluid flow due to the thermophoresis and gyrotactic microorganism between the gap of a disk and cone. *Braz. J. Phys.* **2021**, *51*, 687–697. [CrossRef]
41. Ahmad, I.; Ilyas, H.; Urooj, A.; Aslam, M.S.; Shoaib, M.; Raja, M.A.Z. Novel applications of intelligent computing paradigms for the analysis of nonlinear reactive transport model of the fluid in soft tissues and microvessels. *Neural Comput. Appl.* **2019**, *31*, 9041–9059. [CrossRef]
42. Shoaib, M.; Raja, M.A.Z.; Sabir, M.T.; Bukhari, A.H.; Alrabaiah, H.; Shah, Z.; Kumam, P.; Islam, S. A stochastic numerical analysis based on hybrid NAR-RBFs networks nonlinear SITR model for novel COVID-19 dynamics. *Comput. Methods Programs Biomed.* **2021**, *202*, 105973. [CrossRef]
43. Shah, Z.; Raja, M.A.Z.; Shoaib, M. Design of Bayesian stochastic networks for numerical treatment of Williamson fluid stretching flow model with mixed convected heat generation. *Numer. Heat Transf. Part B Fundam.* **2024**, 1–24. [CrossRef]
44. Farooq, U.; Waqas, H.; Fatima, N.; Imran, M.; Noreen, S.; Bariq, A.; Galal, A.M. Computational framework of cobalt ferrite and silver-based hybrid nanofluid over a rotating disk and cone: A comparative study. *Sci. Rep.* **2023**, *13*, 5369. [CrossRef] [PubMed]
45. Ahmadi, M.H.; Mohseni-Gharyehsafa, B.; Ghazvini, M.; Goodarzi, M.; Jilte, R.D.; Kumar, R. Comparing various machine learning approaches in modeling the dynamic viscosity of CuO/water nanofluid. *J. Therm. Anal. Calorim.* **2020**, *139*, 2585–2599. [CrossRef]
46. Ali, A.; Ahammad, N.A.; Tag-Eldin, E.; Gamaoun, F.; Daradkeh, Y.I.; Yassen, M.F. MHD Williamson nanofluid flow in the rheology of thermal radiation, Joule heating, and chemical reaction using the Levenberg–Marquardt neural network algorithm. *Front. Energy Res.* **2022**, *10*, 965603. [CrossRef]
47. Liu, T.; Li, Y.; Jing, Q.; Xie, Y.; Zhang, D. Supervised learning method for the physical field reconstruction in a nanofluid heat transfer problem. *Int. J. Heat Mass Transf.* **2021**, *165*, 120684. [CrossRef]
48. Raja, M.A.Z.; Shoaib, M.; Khan, Z.; Zuhra, S.; Saleel, C.A.; Nisar, K.S.; Khan, I. Supervised neural networks learning algorithm for three dimensional hybrid nanofluid flow with radiative heat and mass fluxes. *Ain Shams Eng. J.* **2022**, *13*, 101573. [CrossRef]
49. Mishra, S.R.; Baag, S.; Mohapatra, D.K. Chemical reaction and Soret effects on hydromagnetic micropolar fluid along a stretching sheet. *Eng. Sci. Technol. Int. J.* **2016**, *19*, 1919–1928. [CrossRef]
50. Öcal, S.; Gökçek, M.; Çolak, A.B.; Korkanç, M. A comprehensive and comparative experimental analysis on thermal conductivity of TiO_2-$CaCO_3$/Water hybrid nanofluid: Proposing new correlation and artificial neural network optimization. *Heat Transf. Res.* **2021**, *52*, 55–79. [CrossRef]
51. Amin, M.; Awwad, F.A.; Ismail, E.A.; Ishaq, M.; Gul, T.; Khan, T.S. Quantitative analysis of the electromagnetic hybrid nanofluid flow within the gap of two tubes using deep learning neural networks. *Multidiscip. Model. Mater. Struct.* **2024**, *20*, 671–687. [CrossRef]
52. Alotaibi, A.; Gul, T.; Saleh Alotaibi, I.M.; Alghuried, A.; Alshomrani, A.S.; Alghuson, M. Artificial neural network analysis of the flow of nanofluids in a variable porous gap between two inclined cylinders for solar applications. *Eng. Appl. Comput. Fluid Mech.* **2024**, *18*, 2343418. [CrossRef]
53. Nasir, S.; Berrouk, A.S.; Gul, T. Analysis of chemical reactive nanofluid flow on stretching surface using numerical soft computing approach for thermal enhancement. *Eng. Appl. Comput. Fluid Mech.* **2024**, *18*, 2340609. [CrossRef]